



Relationship between Region 2 field-aligned current and the ring current: Model results

Y. Zheng,¹ A. T. Y. Lui,¹ M.-C. Fok,² B. J. Anderson,¹ P. C. Brandt,¹ T. J. Immel,³ and D. G. Mitchell¹

Received 8 January 2006; revised 21 July 2006; accepted 1 August 2006; published 19 October 2006.

[1] Detailed investigations on the relationship between the ring current and Region 2 field-aligned currents (FACs) have been tenuous. Using the Comprehensive Ring Current Model (CRCM), we first studied their relationship for two GEM storm events (22 April 2001 and 21 October 2001) through model and data comparison. The simulated Region 2 FACs for two different magnetic storm events capture major characteristics of the Iridium measurements, and the simulated ENA flux has a reasonable agreement with the IMAGE/HENA data. We then examined the effects of polar cap potential drop, ionospheric conductivity, plasma sheet density and different magnetic field models on the development of Region 2 FACs, and the relationship between Region 2 FACs and the ring current, either through one of the two GEM events or the 12 August 2000 storm. It is shown that an increase in polar cap potential, ionospheric conductivity, or plasma sheet density generally results in an increase in Region 2 FACs' intensity, but Region 2 FACs display different local time and latitudinal distributions for changes in each parameter due to the different mechanisms involved. The CRCM run in the Tsyganenko 2004 magnetic field model for storm times (T04S), which includes a partial ring current, produces the dawn-dusk asymmetry in Region 2 FACs during geomagnetically active times, as reported by Anderson et al. (2005): more intense currents flow into the ionosphere around dusk, compared to those that flow out of the ionosphere around dawn, and the dusk currents shift further equatorward than do the dawn currents.

Citation: Zheng, Y., A. T. Y. Lui, M.-C. Fok, B. J. Anderson, P. C. Brandt, T. J. Immel, and D. G. Mitchell (2006), Relationship between Region 2 field-aligned current and the ring current: Model results, *J. Geophys. Res.*, *111*, A11S06, doi:10.1029/2006JA011603.

1. Introduction

[2] Both ring current and field-aligned currents (FACs) have been areas of active research for decades and are major components in the magnetosphere-ionosphere (M-I) coupling. All previous theoretical considerations have reached the same conclusion, namely, that an azimuthal pressure gradient in the inner magnetosphere is the main driver of the Region 2 FACs [Vasyliunas, 1970; Southwood, 1977; Harel et al., 1981]. Therefore an inseparable relationship exists between the ring current and Region 2 FACs, influenced both by solar wind and by ionosphere conditions.

[3] The Region 1 and Region 2 currents behave differently in response to geomagnetic activities because the sources of the Region 2 currents are quite different from those of the Region 1 currents [Iijima and Potemra, 1978; Tanaka, 1995]. The ionospheric map of the statistical FAC

distribution during moderate magnetic conditions was first derived by Iijima and Potemra [1978], using TRIAD observations. Their result shows that equatorward of the Region 1 current, the Region 2 FACs go into the ionosphere in the dusk sector and out of the ionosphere in the dawn sector, opposite to the direction of the Region 1 current. The response of field-aligned current intensity to changes of the interplanetary quantities has been broadly studied in the past [e.g., Zanetti et al., 1983; Iijima, 1984; Erlandson et al., 1988]. It is also known that FACs have a seasonal dependence [e.g., Fujii and Iijima, 1987; Ohtani et al., 2005]. Using Iridium data, Anderson et al. [2002] finds that the intensity of the currents is higher for southward IMF (Interplanetary Magnetic Field) than for northward IMF. The centroid position of the field-aligned currents expands equatorward when the IMF turns southward and poleward when the IMF turns northward.

[4] The intensification of the ring current is a primary feature of magnetic storms that cause world-wide depression of the geomagnetic field. The ring current dynamics is a key element of magnetospheric physics. Considerable progress on particle sources, transport, composition, decay and global distribution/morphology of the ring current has been made through numerical simulations (see reviews by

¹Johns Hopkins University Applied Physics Laboratory, Laurel, Maryland, USA.

²NASA Goddard Space Flight Center, Greenbelt, Maryland, USA.

³Space Sciences Laboratory, University of California, Berkeley, California, USA.

Ebihara and Ejiri [2002] and *Jordanova*, [2003]) and observations [e.g., *Daglis et al.*, 1999; *Brandt et al.*, 2002]. However, detailed studies on the relationship between the ring current and Region 2 FACs are almost nonexistent. In this paper we study this relationship by means of numerical simulation using the comprehensive ring current model (CRCM), which takes Magnetosphere-Ionosphere (M-I) coupling into consideration [*Fok et al.*, 2001a].

[5] Global numerical modeling is a powerful tool for understanding the complexity of a highly dynamic region such as the ring current and its coupling to the ionosphere. Various computational models of ring current particle dynamics have been developed. The most successful computer simulations of storm-time ring current injection have assumed that the mechanism of earthward plasma transport is adiabatic drift in a time-varying electric field [e.g., *Ejiri et al.*, 1978; *Wolf et al.*, 1982; *Chen et al.*, 1993, 1994; *Jordanova et al.*, 1997; *Fok et al.*, 1993, 1996, 1999]. The plasma source strength and the convective drift strength are considered to be two primary controlling factors in the storm-time ring current [*Kozyra and Liemohn*, 2003]. The plasma sheet is an essential participant in magnetic storm dynamics as a reservoir of ring current particles. Other processes contributing to the ring current dynamics are radial diffusion [e.g., *Chen et al.*, 1994] and substorm-induced electric field [e.g., *Fok et al.*, 1996, 1999]. The ring current decay and loss mechanisms have also been successfully modeled [*Fok et al.*, 1993; *Liemohn et al.*, 1999].

[6] In the existing models of M-I coupling, important early analytical models include the one developed by *Vasyliunas* [1970, 1972], which provides a theoretical description of the M-I coupling, and the one by *Senior and Blanc* [1984], which considers spatial distribution of the ionospheric conductivity. More comprehensive numerical models which take the complex electrodynamics of the M-I coupling into account have been very few; they include the Rice Convection Model (RCM) developed by *Wolf* and his coworkers [*Wolf*, 1970; *Jaggi and Wolf*, 1973; *Harel et al.*, 1981; *Spiro et al.*, 1981; *Wolf et al.*, 1982; *Spiro and Wolf*, 1984; *Toffoletto et al.*, 2003] and the Magnetosphere-Thermosphere-Ionosphere Electrodynamics General Circulation Model (MTIE-GCM) [*Peymirat et al.*, 1998, 2000].

[7] All of the present ring current models and those including the M-I coupling have well-known strengths and deficiencies. Each treats some areas of physics in a detailed and complete manner, while some processes are parameterized crudely. Ideally, a complete model should contain as few *ad hoc* assumptions and adjustable coefficients as possible. The Comprehensive Ring Current Model (CRCM), which couples the Rice Convection Model (RCM) and the kinetic model of *Fok* and coworkers, approaches such a model [*Fok et al.*, 2001a]. The coupled model, with the strength of the two parent models, provides a powerful tool in simulating storm-time ring current dynamics. It allows a self-consistently calculated electric field, resulting from the M-I coupling, to be utilized in solving the kinetic equation of the ring current plasma. The CRCM is like the RCM but with complete pitch angle distributions, and it can adopt different magnetic field models. It has successfully reproduced many observational features of the ring current [*Fok et al.*, 2001a, 2003;

Ebihara et al., 2004, 2005]. Besides its success in modeling ring current dynamics, it is one of the very few models which also provide Region 2 FACs in the ionosphere, as most ring current models do not include M-I coupling. The CRCM differs from the MTIE-GCM in that the latter relies completely on the fluid approach while the CRCM treats ring current particles kinetically. The MTIE-GCM also uses a less realistic dipole magnetic field model.

[8] Region 2 FACs were reported to have a linear dependence on the dawn-dusk component of the interplanetary electric field (IEF). However, the dependence of the FAC intensity on the IEF had on average twice the slope for the sunlit side as for the dark side, a fact which was explained in terms of difference in Pedersen conductivity [*Russell and Fleishman*, 2002]. Both solar wind and IMF parameters and ionospheric conductivity are thus shown to affect the Region 2 FACs [e.g., *Wang et al.*, 2005].

[9] The specific question we want to address here is how various factors, such as the polar cap potential, ionospheric conductivity, plasma sheet density, and different magnetic field models, individually affect the morphology and intensity of Region 2 FACs and how they relate to ring current in terms of spatial distribution, temporal characteristics, intensity, etc.

[10] This paper consists of five sections. The CRCM is described briefly in section 2, followed by section 3 which includes our simulation results of two GEM events (22 April 2001 and 21 October 2001). Comparisons both between the two events and with the data are made. After the demonstration of the reasonable agreement between the model results and observations, we explore the effects of different physical parameters on the evolution of Region 2 FACs and their relationship with the ring current in section 4: with the polar cap potential in section 4.1, ionospheric conductivity in section 4.2, plasma sheet density in section 4.3, different magnetic field models (*Tsyganenko 96* [*Tsyganenko*, 1995] and *Tsyganenko 2004* during storm times [*Tsyganenko and Sitnov*, 2005]) in section 4.4. Section 5 discusses and summarizes the results. The goal of this paper is to better our understanding of physical mechanisms involved in the relationship between the ring current and Region 2 FACs, which is difficult or impossible to achieve with data at the present time.

2. CRCM

[11] Here we give a brief description of the CRCM and the initial and boundary conditions used in the study. The details of the model are given by *Fok et al.* [2001a] and a diagram of the model logic to illustrate the M-I coupling is provided by *Ebihara et al.* [2004].

2.1. Kinetic Equation Used By Fok Ring Current Model

[12] The Fok ring current model is based on solving the bounce-averaged Boltzmann equation in space and time, that is

$$\frac{\partial \bar{f}_s}{\partial t} + \langle \dot{l}_i \rangle \frac{\partial \bar{f}_s}{\partial l_i} + \langle \dot{\phi}_i \rangle \frac{\partial \bar{f}_s}{\partial \phi_i} = -\nu \sigma_s \langle n_H \rangle \bar{f}_s - \left(\frac{\bar{f}_s}{0.5 \tau_b} \right)_{\text{loss_cone}} \quad (1)$$

where $\bar{f}_s = \bar{f}_s(l_i, \varphi_i, M, K)$ is the four-dimensional phase space density, l_i is the magnetic latitude at ionospheric altitude ($r_i \approx 1.02 R_E$), φ_i is the magnetic local time at the ionospheric altitude, M and K are two adiabatic invariants, ν is the velocity of particles, σ_s represents the cross section for charge exchange, n_H is the hydrogen density, and τ_b is the bounce period. The operation $\langle \rangle$ means a bounce average over a field line between two mirror points. The loss cone altitude is at 120 km.

[13] The bounce averaged drift velocities, $\langle \dot{l}_i \rangle$ and $\langle \dot{\varphi}_i \rangle$, are given as follows [Fok and Moore, 1997]:

$$\langle \dot{l}_i \rangle = -\frac{1}{qG} \frac{\partial H}{\partial \varphi_i} \quad (2)$$

$$\langle \dot{\varphi}_i \rangle = \frac{1}{qG} \frac{\partial H}{\partial l_i} \quad (3)$$

where $G = M_E \sin(2l_i)/r_i$ and M_E is the Earth's dipole magnetic moment and q is the charge. The Hamiltonian H is given by

$$H = W + q\Phi - \frac{q\Omega M_E}{2r_i} \cos 2l_i \quad (4)$$

where W is the particle kinetic energy, Φ is the electric potential and Ω is the angular velocity of the Earth's rotation. The right-hand side of equation (4) represents magnetic drift, including gradient \mathbf{B} and curvature drifts, the $\mathbf{E} \times \mathbf{B}$ convection drift and the drift by the corotation electric field, respectively. The Fok model allows tracking particle motion in a nondipolar magnetic field, with an arbitrary pitch angle distribution. The same physical principles can be applied to model the radiation belt particles as well [Fok et al., 2001b; Zheng et al., 2003].

2.2. RCM Algorithm of Field-Aligned Current and the Electric Field

[14] The RCM algorithm is used to connect the ring current particles in the magnetosphere to the field-aligned currents in the ionosphere based on two conservation laws: conservation of number of particles and the current.

[15] The phase space density $\bar{f}_s = \bar{f}_s(l_i, \varphi_i, M, K)$ is converted to $\eta(l_i, \varphi_i, M, K)$, which represents the number of particles per unit magnetic flux in the ranges of $(M, M + \Delta M)$, $(K, K + \Delta K)$. The relation is

$$\eta = 4\sqrt{2}\pi m_0^{3/2} \bar{f}_s M^{1/2} \Delta M \Delta K \quad (5)$$

[16] The field-aligned current is then given by

$$\frac{J_{\parallel i}}{B_i} = \sum_j \frac{B}{B^2} \cdot (\nabla \eta_j \times \nabla W_j) \quad (6)$$

which can be rewritten as

$$J_{\parallel i} = \frac{1}{r_i^2 \cos l_i} \sum_j \left(\frac{\partial \eta_j}{\partial l_i} \frac{\partial W_j}{\partial \varphi_i} - \frac{\partial \eta_j}{\partial \varphi_i} \frac{\partial W_j}{\partial l_i} \right) \quad (7)$$

where index i represents quantities evaluated at ionosphere altitude (r_i) and index j represents different species.

[17] The ionospheric Φ_i (therefore the electric field) can be obtained by solving the Poisson equation

$$\nabla \cdot (-\Sigma \cdot \nabla \Phi_i) = J_{\parallel i} \sin I \quad (8)$$

where Σ is the height-integrated conductance tensor and I is the magnetic dip angle.

[18] The ionospheric electric potential Φ_i calculated by equation (8) is mapped along magnetic field lines using the assumption that the field line is equipotential. The newly updated electric field is then used to solve the kinetic equation of ring current particles (equation (1)).

[19] The ionospheric conductance Σ includes contributions both from solar irradiance (background) and from the auroral particle precipitation [Ebihara et al., 2004]. The International Reference Ionosphere (IRI-95) [Bilitza, 1997] and the Mass Spectrometer Incoherent Scatter (MSIS-E90) model are used to calculate the background conductance. The universal time dependence of conductance is not included. In default, the Hardy model is used for calculating the auroral conductance, which is K_p dependent [Hardy et al., 1987]. We sometimes use a more realistic precipitating conductance based on observations when available, such as the one obtained using data from the far ultraviolet imager (FUV) aboard the IMAGE satellite [Mende et al., 2000a, 2000b].

2.3. Initial and Boundary Conditions

[20] The initial particle distribution in the magnetosphere is based on AMPTE/CCE observations under quiet times [Sheldon and Hamilton, 1993].

[21] The outer boundary of the ionosphere for the Poisson equation (8) is located at 66.7° at 100 km altitude. The cross polar cap potential at the boundary is given by the Weimer 2000 model [Weimer, 2001]. The boundary of the magnetosphere for particle injection is located at the radial distance of $10 R_E$ in the equatorial plane. Only protons are considered here. The distribution function of the injected particles is assumed to be Maxwellian and solar wind dependent, with density and characteristic energy driven by solar wind density and velocity as follows [Borovsky et al., 1998]:

$$N_{PS}(t) = 0.025 \bullet N_{SW}(t - 3hr) + 0.395 \quad (9)$$

$$E_o(t) = 0.019 \bullet V_{SW}(t - 3hr) - 3.65 \quad (10)$$

where N_{PS} is the plasma sheet density in cm^{-3} and N_{SW} is the solar wind density in cm^{-3} . V_{SW} is the solar wind speed in km/s and E_o is in unit of keV. Notice there is a 3-hour time lag between the solar wind and the nightside boundary. The boundary condition on the dayside is not important and is modeled in a simple manner. The dayside boundary distribution is assumed to be a Maxwellian with constant temperature (0.3 keV) and density (5 cm^{-3}). The boundary conditions are set as above under default.

2.4. Limitations and Assumptions of the CRCM

[22] Despite the fact that CRCM is a powerful model which self-consistently calculates the electric field, it has its own limitations: the ionospheric conductance is not explic-

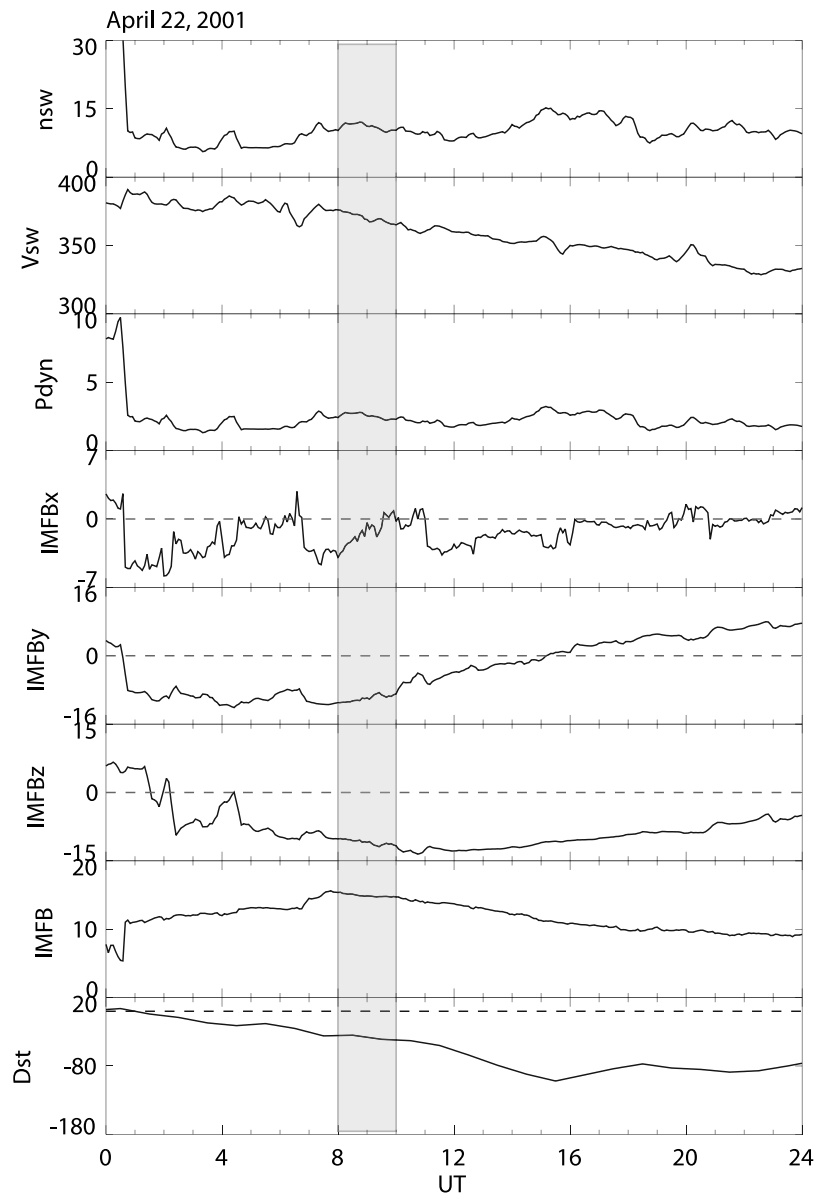


Figure 1. Solar wind and IMF conditions measured by ACE spacecraft (time-shifted by 1 hour), along with the Dst index for the 22 April 2001 event. From top to bottom are: density in cm^{-3} , solar wind speed in km/s, solar wind dynamic pressure in nPa, three components of the IMF in nT in GSM coordinates. The highlighted region in Figure 1 is used for data and model comparison.

itly tied to the distribution of magnetospheric particles or their precipitation patterns; there is no parallel electric field in the consideration of M-I coupling (i.e., magnetic field lines are equipotential lines); it employs an externally imposed magnetic field model (i.e., the model is not magnetically self-consistent yet). It should be mentioned that calculating magnetic fields in a self-consistent manner still remains a big challenge in ring current modeling.

3. Simulation Results of Region 2 FACs for Two GEM Events

[23] The default magnetic field model for the CRCM runs is the Tsyganenko 96 model [Tsyganenko, 1995] and it is referred to as the T96 model. The T96 model provides the external magnetic field parameterized by the solar wind

dynamic pressure, the Dst index, IMF B_y , and IMF B_z . In this section, general default settings of the CRCM are used to simulate two GEM events: 22 April 2001 and 21 October 2001. The focus of our analysis is on the Region 2 FACs.

[24] The solar wind and IMF conditions, along with the Dst values, are shown in Figure 1 and Figure 2, with Figure 1 of the 22 April 2001 event and Figure 2 of the 21 October 2001 event. They bear the same format as the top seven panels measured from the ACE spacecraft (with 1-hour time shift applied), while the bottom panel shows the hourly Dst index. The three components of IMF are in GSM coordinates. The April event is a moderate storm with minimum Dst value of -102 nT and the October event represents a relatively large storm with its minimum Dst value reaching -187 nT. For the simulation results shown in this section, the magnetic field configuration based on the

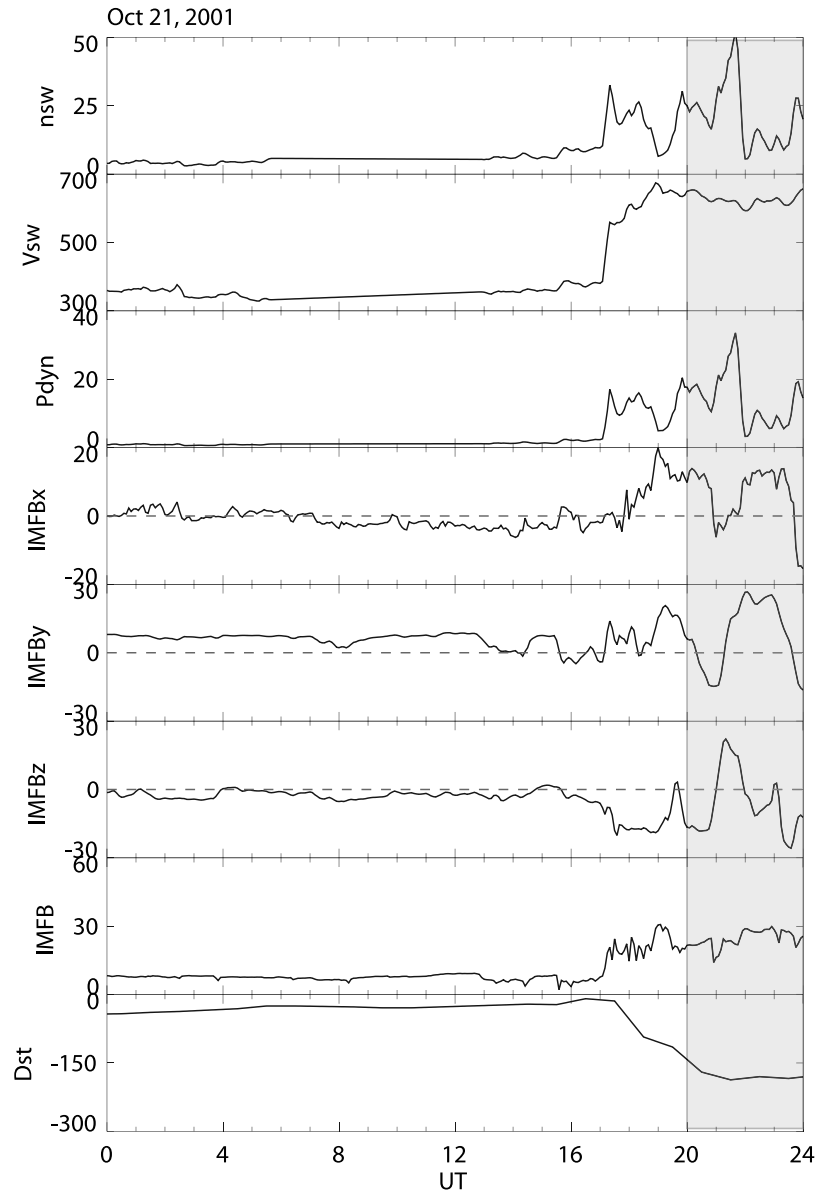


Figure 2. Same format as Figure 1, but for the 21 October 2001 event.

T96 model is updated every 10 min according to the ACE measurements shown in Figures 1 and 2.

[25] Figure 3 shows the input boundary conditions for both events, with the 22 April 2001 event shown in the top plot and the 21 October 2001 event in the bottom. Two very important boundary parameters are represented here: the polar cap potential drop and the plasma sheet density at $10 R_E$ derived from equation (9). The highlighted regions are the intervals during which Iridium data display self consistent perturbation distributions and are used to derive Birkeland currents. We therefore focus our data and model comparison on these intervals. For the April event, the time interval (0800–1000 UT) is in the early period of the main phase of the storm with Dst value of -30 nT, while for the October event, the two intervals are 2000–2200 UT and 2200–2400 UT, near the Dst minimum with an average Dst of -180 nT.

[26] Figure 4 shows the data and model comparison for the three intervals mentioned above, with the first column showing the field-aligned currents (including Region 1 FACs) derived from the Iridium satellite constellation (with data accumulation time of 2 hours), the second column showing mostly the Region 2 FACs from the Iridium data (for easy comparison with the simulation results in the third column), the third column showing the field-aligned current calculated from the CRCM, and the corresponding Pedersen conductivity used for the run shown on the rightmost column. The model result/input shown in the third and fourth columns is averaged over the 2-hour interval to be consistent with the Iridium data. For all the plots, noon is at the top and dusk is to the left. The same color bar for the FAC is used throughout the paper unless otherwise mentioned. Procedures for processing Iridium magnetic field data and evaluating field-aligned currents from the pro-

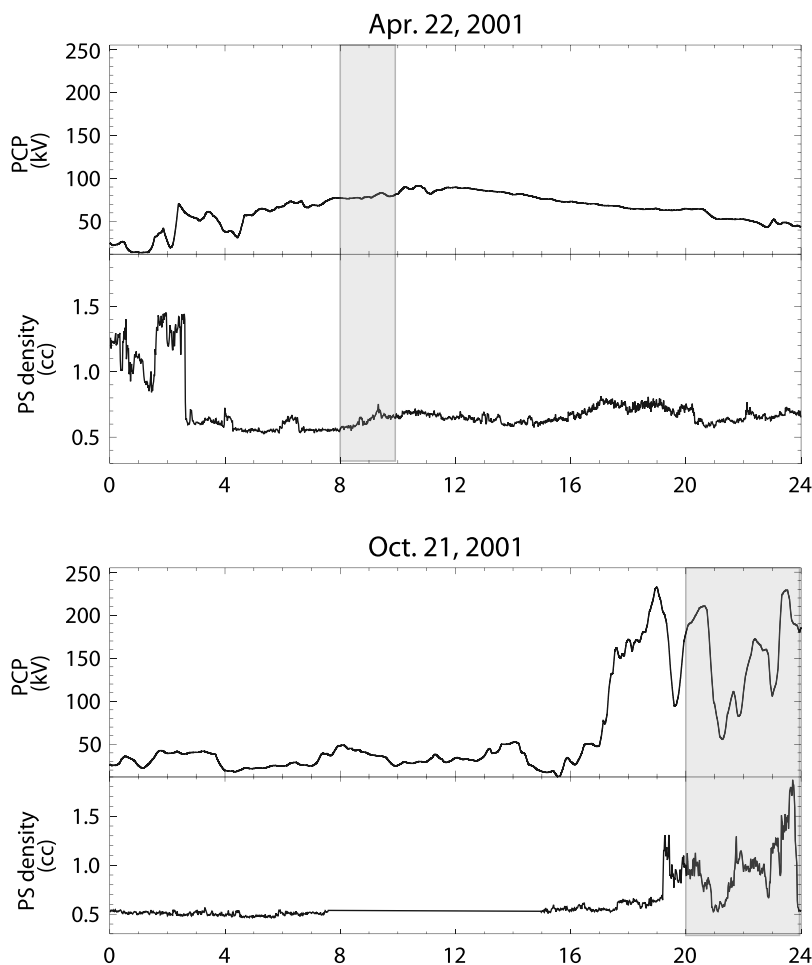


Figure 3. Input boundary conditions for both events, with the 22 April 2001 event shown in the top plot and the 21 October 2001 event on the bottom. Two very important boundary parameters are shown here: the polar cap potential drop and the plasma sheet density at $10 R_e$ derived from equation (9). The highlighted regions are the interval during which model and data comparisons are made.

cessed data were documented by *Anderson et al.* [2000] and *Waters et al.* [2001]. The Iridium field-aligned currents have been compared with MHD simulations [*Korth et al.*, 2004] showing that the resolution of the simulation grid is critical to representing the currents and that the ionospheric conductance plays a significant role in the simulation results even for the Region 1 currents. As expected, *Korth et al.* [2004] also finds that the Region 2 currents are under represented in the MHD simulation since the ring current physics was not included in the MHD simulations they used. Since the CRCM does not have Region 1 FACs, we focus our comparison on the Region 2 FACs only.

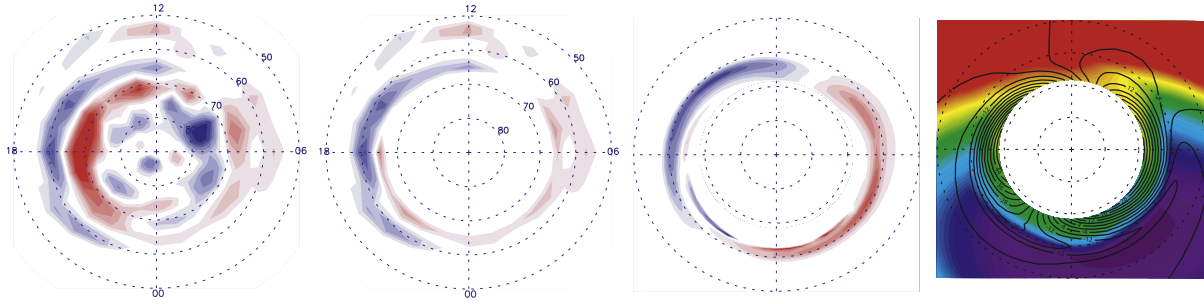
[27] By mainly comparing the second column (Region 2 FACs of Iridium) with the third column (Region 2 FACs from the CRCM) in Figure 4, we can see that the comparison between data and simulation is not perfect: the model did not reproduce the fine structured currents between 50° and 60° ; there is also disagreement in latitudinal extent and local time distribution of Region 2 FACs between the model and the Iridium data. However, Figure 4 shows that under default settings, the CRCM is able to capture major characteristics of Region 2 FACs such as the equatorward expansion and greater intensity of Region 2 FACs shown

in the October event. Some features of the intensity and local time evolution of Region 2 FACs are also reproduced, such as the enhancement at 1800 MLT and in the early morning sector during the interval of 2200–2400 UT on 21 October 2001.

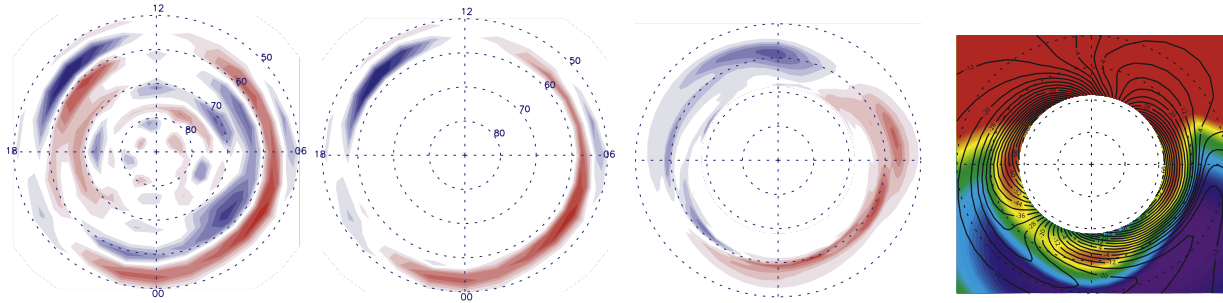
[28] To help understand the differences between the two events, the electric field map of the ionosphere is plotted in Figure 5 for 0900 UT on 22 April 2001, 2100 UT and 2300 UT on 21 October 2001. The arrow is used to indicate the direction and the magnitude of the electric field, with the color contour showing its magnitude. The flow reversal region due to ring current shielding (the near white color trace from 1800–0600 MLT in the nightside) is at a lower latitude for the October event than for the April event. The two times in the October event have a large electric field that penetrates deeper to lower latitudes.

[29] Figure 6 is shown here to connect the Region 2 FAC behavior with the characteristics of ring current. The left column shows the equatorial flux of the 44 keV protons, while the right column is the perpendicular pressure in the equatorial plane due to particles in the energy range of 1–180 keV. The times are same as those in Figure 5. X and Y axes represents x, y in solar magnetic coordinates (SM)

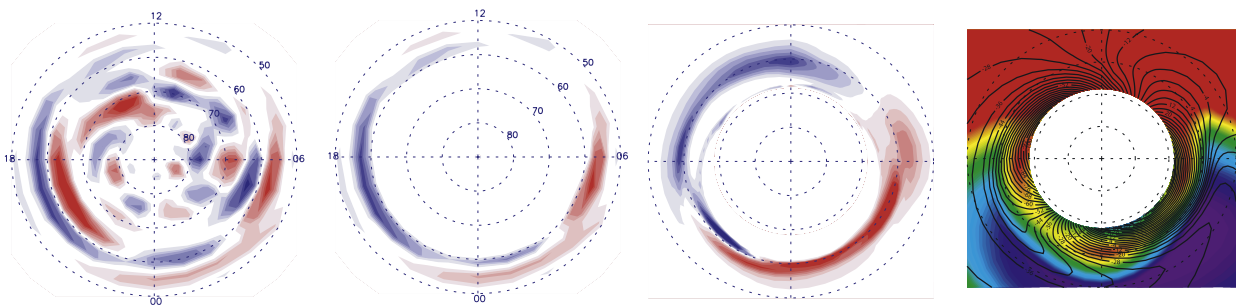
04/22/2001 08:00 - 10:00 UT



10/21/2001 20:00 - 22:00 UT



10/21/2001 22:00 - 24:00 UT



(a) Iridium/all

(b) Iridium/R2 FACs

(c) Simulated R2 FACs

(d) Conductance

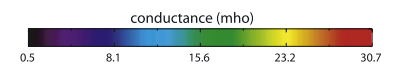
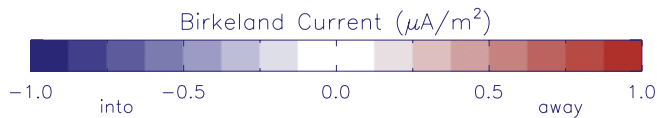


Figure 4. The data and model comparison for the three intervals (0800–1000 UT on 22 April 2001, 2000–2200 UT and 2200–2400 UT on 21 October 2001), with the first column showing the field-aligned current derived from the Iridium satellite constellation (with data accumulation time of 2 hours), the second column showing mainly Region 2 FACs from Iridium, the third column showing the field-aligned current calculated from the CRCM, and the corresponding Pedersen conductivity used for the run shown on the rightmost column. Noon is at the top and dusk is to the left.

respectively, in unit of R_E . We can see that during the main phase of the October storm, the 44 keV protons penetrated more deeply into the inner magnetosphere with higher fluxes comparing to the April event. Correspondingly, the perpendicular pressure peaks around $2.5 R_E$ for the October

event, while it peaks around $4.5 R_E$ in the April event with a much smaller magnitude. The pressure is so weak (about 2 nPa, rather isotropic about local time) in the April event that it blends into the background color.

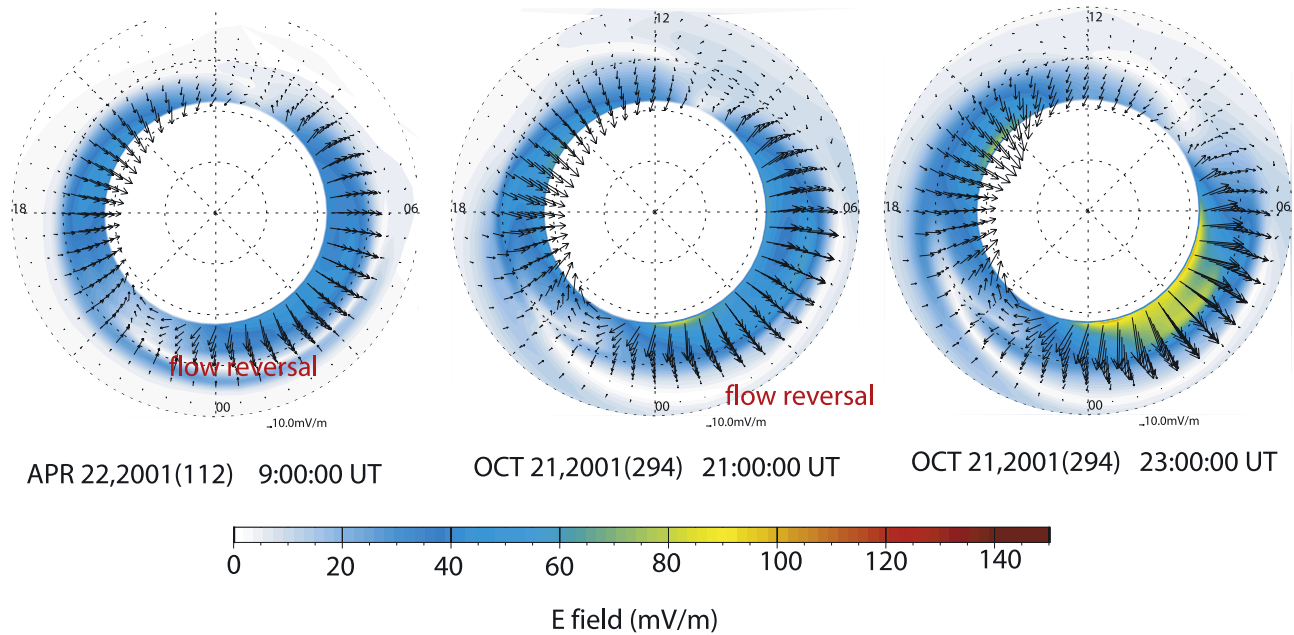


Figure 5. The electric field map in the ionosphere for 0900 UT on 22 April 2001, 2100 UT, and 2300 UT on 21 October 2001. The arrow is used to indicate the direction and the magnitude of the electric field, with the color contour showing its magnitude.

[30] Equations (6) and (7) show that FACs are closely related to ring current particle characteristics. They are functions of the gradients of numbers per magnetic flux $\eta(l_i, \phi_i, M, K)$ and particle energy W . At the same time, they are affected by the magnetic field configuration [e.g., *Vasyliunas, 1970*]. Here $\eta(l_i, \phi_i, M, K)$ is affected by multiple factors, such as the global electric field and the plasma sheet particle source strength for the ring current. The global electric field pattern is controlled by polar cap potential drop and ionospheric conductivity. Therefore as a result of the complex interactions of ring current and the ionosphere, the Region 2 FACs depend on many different parameters. The simulation of two GEM events shows that the Region 2 FACs are stronger and expands further equatorward when there is a stronger, deeper penetrated ring current.

[31] Figure 7 shows the simulated proton flux (left column), hydrogen (H) ENA (energetic neutral atoms) flux (middle column) and the measured hydrogen ENA flux (right column) from the High-Energy Neutral Atom (HENA) imager onboard the IMAGE spacecraft [*Mitchell et al., 2000*] in the energy range of 39–50 keV, with the top row showing the April event at 0800 UT and the bottom row showing the October event at 2000 UT. Details on how to calculate hydrogen ENA flux through the simulated ion flux can be found in the work of *Ebihara and Fok [2004]*. The simulated ENA flux of the October event has a very good agreement with the IMAGE/HENA data, showing the ENA emission peaking in the premidnight and extending all the way to postmidnight \sim 0500 MLT. However, the simulated H ENA flux for the April event at 0800 UT is weaker than the measurements but the peak of the ENA emission was captured well in the simulation (the peak was located premidnight). The equatorial proton fluxes displayed on the left again show that ring current had a deeper penetration

during the main phase of the intense October storm than during the early stage of the moderate April storm.

[32] The simulation of the two GEM events under default conditions and its general agreement with both Iridium data and the IMAGE/HENA data show that the CRCM is a useful tool in studying ring current dynamics and its electrodynamic coupling to the ionosphere. Therefore in section 4 we aim to elucidate the physical mechanisms involved in the relationship of Region 2 FACs and the ring current by the exploration of parameter space, such as polar cap potential drop, ionospheric conductivity, plasma sheet density, magnetic field configuration, etc.

4. Several Physical Parameters' Influence on Region 2 FAC

4.1. Effects of Polar Cap Potential on Region 2 FAC

[33] Polar cap potential drop is a key parameter for understanding solar wind-magnetosphere-ionosphere coupling. It depends both on solar wind driving and on the feedbacks from the Region 1 current system [*Siscoe et al., 2002*] and is therefore a very important factor in determining the ring current response to the solar wind driving. A proper representation of polar cap potential at the high latitude boundary of the CRCM can partly complement the lack of Region 1 currents in the model. The strength, as well as the temporal and spatial behavior of the polar cap potential, has dramatic effects in controlling the global electric field distribution [*Senior and Blanc, 1984; Fejer et al., 1990; Spiro et al., 1988; Peymirat et al., 2000*]. In this section, we investigate the effects of polar cap potential at the high latitude boundary on the development of Region 2 FACs. The 21 October 2001 event is taken as an example.

[34] Three runs were completed with case (a) polar cap potential drop being half of what is obtained through the

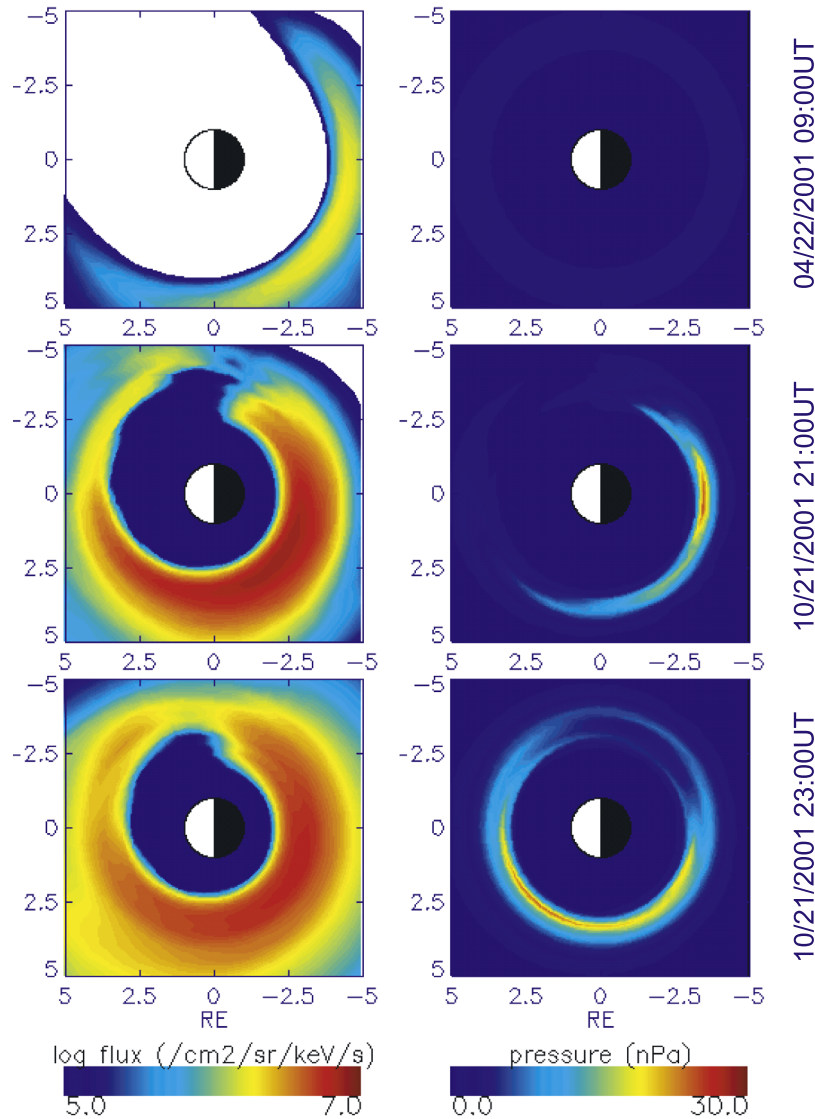


Figure 6. The left column shows the equatorial flux of the 44 keV protons, while the right column is the perpendicular pressure in the equatorial plane due to particles in the energy range of 1–180 keV. The times are same as those in Figure 5.

assimilative mapping of ionospheric electrodynamics (AMIE) model [Richmond, 1992] (the dashed line in Figure 8), case (b) polar cap potential drop derived from the AMIE model (the dotted line in Figure 8), and case (c) polar cap potential obtained from the Weimer 2000 model (the solid line in Figure 8). All the other input parameters are taken as default. The average polar cap potential value over the 1-day interval is 42.2 kV, 84.5 kV, and 68.0 kV for case (a), (b), and (c) respectively.

[35] The top panel of Figure 9 shows the FACs from the three simulation runs at 20:00 UT (All three cases share the same color bar as in Figure 4). The bottom ones are the simulated ionospheric electric field maps for the three cases at the same time (The same color bar is used for all cases as appeared in Figure 5). From a comparison, we can see that case (b), with a higher average polar cap potential, results in higher Region 2 FACs than both case (a) and case (c). Region 2 FACs are smaller in general in case (a) due to a small polar cap potential. It is interesting to note that even

though the average value of cases (b) and (c) is similar, there are differences in both the electric field map and the corresponding distribution of Region 2 FACs. The results indicate that Region 2 FACs depend both on overall strength (also corresponding to long-time average of solar wind driving) and instantaneous values of polar cap potential.

[36] To compare Region 2 FACs from the three runs in a quantitative fashion, Figure 10 shows the magnetic local time distribution of the total Region 2 FACs in the ionosphere integrated between the magnetic latitude 40° – 60° (in Ampere) at six different universal times (1700 UT, 1800 UT, 1900 UT, 2000 UT, 2100 UT, and 2200 UT). The Region 2 FAC at different local times is calculated as follows.

$$j_i(\varphi_i) = \int_{l_i=40^\circ}^{l_i=60^\circ} J_i \cdot r_i^2 \cdot \cos l_i \cdot dl_i \cdot d\varphi_i \quad (11)$$

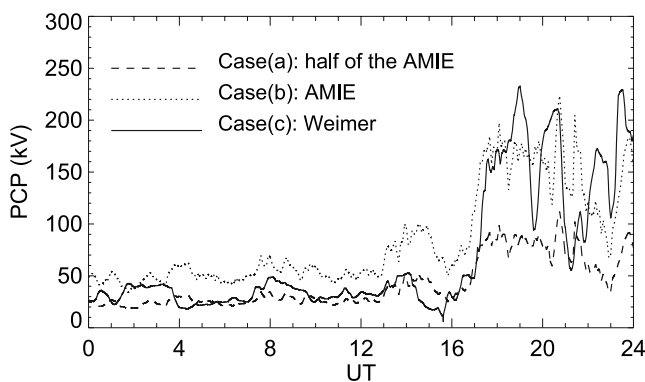


Figure 8. Polar cap potential profiles for three runs. The dotted line represents the polar cap potential derived from the AMIE model (case (b)). The dashed line represents case (a) where the polar cap potential values are half as in case (b). The solid line represents the polar cap potential obtained from the Weimer 2000 model. The average polar cap potential value over the 1-day interval is 42.2 kV, 84.5 kV, and 68.0 kV for case (a), (b) and (c) respectively.

[37] The dashed line is for case (a), the dotted line is for case (b) and the solid line is for case (c). The polar cap potential values for (a) are half of those in (b). Comparing the dashed line and the dotted line, we can see that Region 2 FACs' dependence on polar cap potential is nonlinear. Besides the obvious lower FAC values in case (a), the local time distribution between (a) and (b) is also different. Comparisons between case (b) and case (c) indicate that overall case (b) results in a higher FAC intensity at almost all local times. The outflowing Region 2 FAC peaks more towards dayside for case (b), which has a larger average polar cap potential value. Noticeably, the intensity of Region 2 FACs at dawn side is much larger for case (b) than for case (a).

[38] The parametric study of polar cap potential's effect on the Region 2 FACs shows that higher polar cap potential results in a stronger ring current and therefore stronger Region 2 FACs. This in turn results in a stronger twisting of the convection pattern towards postmidnight. Please notice the local time distribution shift between the solid line and dotted line in Figure 10.

4.2. Effects of Ionospheric Conductivity on Region 2 FAC

[39] If the polar cap potential drop can be viewed as an external parameter roughly representing magnetospheric convection strength, the ionospheric conductivity can be viewed as a partially internal parameter of the ionosphere. Ionospheric conductivity, including both the background conductance due to solar EUV radiation and the particle precipitation (mostly from electrons), has been demonstrated to have an influence on the ionospheric convection flow [e.g., Wolf, 1970; Atkinson and Hutchison, 1978; Senior and Blanc, 1984] through modification of the electric field. The importance of conductance on magnetosphere dynamics has

been reported based on MHD simulations [e.g., Ridley *et al.*, 2004] and its effects on ring current have been studied by Ebihara *et al.* [2004] and by Liemohn *et al.* [2005]. However, studies on its role in regulating M-I coupling and its effects on Region 2 FACs are needed. In this section, the evolution of Region 2 FAC due to change in ionospheric conductivity is studied.

[40] For this numerical experiment, we chose the 12 August 2000 event because of the availability of IMAGE/FUV data which are capable of providing an estimate of the auroral conductance with a high temporal resolution of 2 min. This event was extensively simulated before [Ebihara *et al.*, 2004, 2005].

[41] The 12 August 2000 event represents an intense magnetic storm with its minimum reaching -235 nT at 0900 UT. For the reference run, the parameters used are the same as Ebihara *et al.* [2004]. The daily F10.7 value was 194.3×10^4 Jy and the daily Ap index was 123 for calculating the background conductance. The parameters for the T96 model were held constant throughout the simulation with the solar wind dynamic pressure of 4.62 nPa, Dst of -26 nT, IMF B_y being 5.0 nT and IMF B_z being 5.0 nT. These values are based on the ACE measurements at the beginning of the simulation (0000 UT). For the ring current sources at the plasma sheet boundary, we assume a constant density of 0.5 cm^{-3} and a temperature of 5 keV. The polar cap potential drop at the poleward boundary is from the Weimer 2000 model. Most of the parameters were held constant in order to highlight the ionospheric conductance effects.

[42] The conductance due to auroral precipitation for the reference run is from the Hardy model (case a). For comparison, another run is performed with the auroral conductance obtained from the IMAGE/FUV data (case b). The procedure for obtaining the auroral conductance is the same as described by Ebihara *et al.* [2004]. For the comparison run, the auroral conductance was switched from the Hardy model to the realistic one from the FUV data during the period of 0747–1502 UT, when the data were available.

[43] Figure 11 shows the model comparison of the two runs without or with realistic auroral conductance at two selected times (0800 UT on the left and 0900 UT on the right) near the Dst minimum (0900 UT). The first row shows the FAC map of the reference run (with Hardy model); the second row shows the FAC map of the run using IMAGE/FUV data. The third row shows the auroral Pedersen conductance from both hemispheres used for the reference run, and the fourth row is the auroral Pedersen conductance obtained from the IMAGE/FUV data. For this specific event, we can see that the realistic auroral conductance is generally larger than that of the Hardy model, is more broadly distributed over the latitude, and expands in a more equatorward direction. By comparing the top two rows of Figure 11, we see that the outflowing Region 2 FACs have a smaller dayside expansion when the realistic auroral conductance is used. Correspondingly, the electric field pattern has a lesser degree of twist toward dawn.

Figure 7. The simulated proton flux (left column), hydrogen (H) ENA (energetic neutral atoms) flux (middle column), and measured hydrogen ENA flux (right column) from IMAGE/HENA in the energy range of 39–50 keV. The top row shows the April event at 0800 UT, and the bottom row shows the October event at 2000 UT.

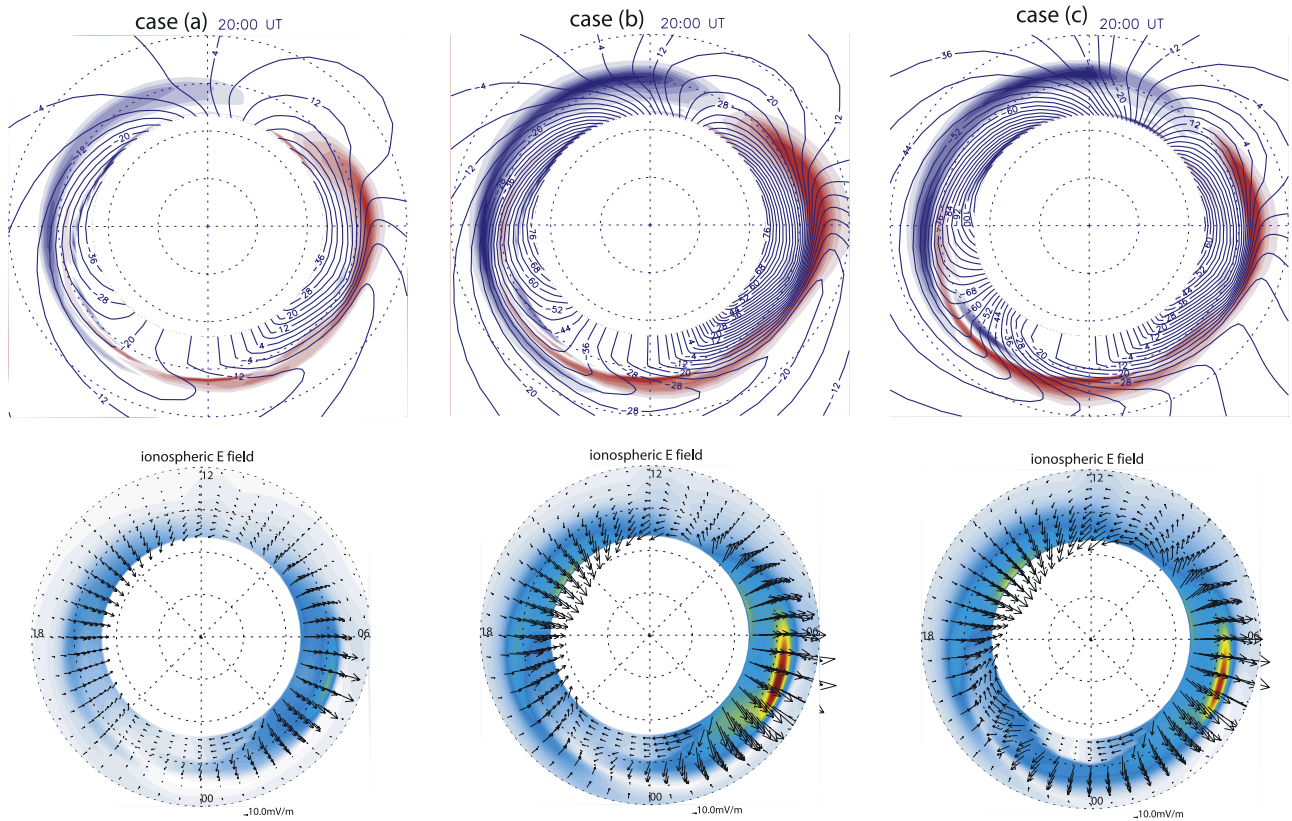


Figure 9. The top panel shows the FACs from the three simulation runs at 2000 UT. The bottom ones are the simulated ionospheric electric field maps for the three runs at the same time (The same color bar is used for all cases, as in Figure 5).

[44] Figure 12 shows the comparison in the format of Figure 10, magnetic local time distribution of Region 2 FACs at different times, with the solid line representing the reference run (case a) and the dashed-dotted line representing the run with FUV data (case b). Figure 13 is the local time distribution of the “equivalent” auroral Pedersen conductance (Σ_{p_equiv}) obtained in a way similar to that of the Region 2 FACs in equation (11). It is integrated over the magnetic latitude range of 40° – 60° .

$$\Sigma_{p_equiv}(\varphi_i) = \int_{l_i=40^\circ}^{l_i=60^\circ} \Sigma_p \cdot r_i^2 \cdot \cos l_i \cdot dl_i \cdot d\varphi_i \quad (12)$$

[45] Judging from Figures 12 and 13, there does not seem to be a one-to-one correspondence between the local distribution of the equivalent Pedersen conductance and Region 2 FACs. What is obvious is that Region 2 FACs have a higher intensity in the run with the realistic auroral conductance. The peak around 0600 MLT in the reference run shifts towards the early morning local time sectors (\sim 0400–0500 MLT) in the comparison run with a more realistic conductance from the FUV data. The local time distribution of the Region 2 FACs is also rather different.

[46] The simulations show that the enhancement of auroral conductivity enables further penetration of convection electric field to lower latitude (see the comparisons between the top two rows of Figure 11) and reduces the shielding

electric field that is fed by the Region 2 FACs. The enhanced auroral conductivity results in a relatively stronger ring current and stronger Region 2 FACs.

[47] Two other runs were performed relative to the reference run: one with the Pedersen conductivity being half of the reference run (case c) and the other with the Pedersen conductivity being twice the reference run (case d). All the parameters were kept the same. The results are shown in Figure 14. The reference run is shown by the solid line (case a) in Figure 14. The dotted line (case c) represents the run whose Pedersen conductance is half of the reference run and the dotted-dashed line (case d) represents the run whose Pedersen conductance is twice the reference run. The comparison between the three runs again indicates that the higher auroral conductance results in more intense Region 2 FACs. The local time distribution of the Region 2 FAC peaks shifts according to the values of the auroral conductance with the negative peak around dawn shifting more toward dayside and the region of downgoing Region 2 FACs (positive) shifting more toward midnight with a small conductance. The peak values of Region 2 FACs do not have a linear dependence of the input auroral conductance, as demonstrated in Figure 14.

4.3. Effects of Plasma Sheet Density on Region 2 FACs

[48] The 12 August 2000 storm is simulated to illustrate the change of plasma sheet density (N_{PS}) on the development of Region 2 FACs. Besides the reference run ($N_{PS} = 0.5 \text{ cm}^{-3}$: case (b)) being performed in section 4.2, we did

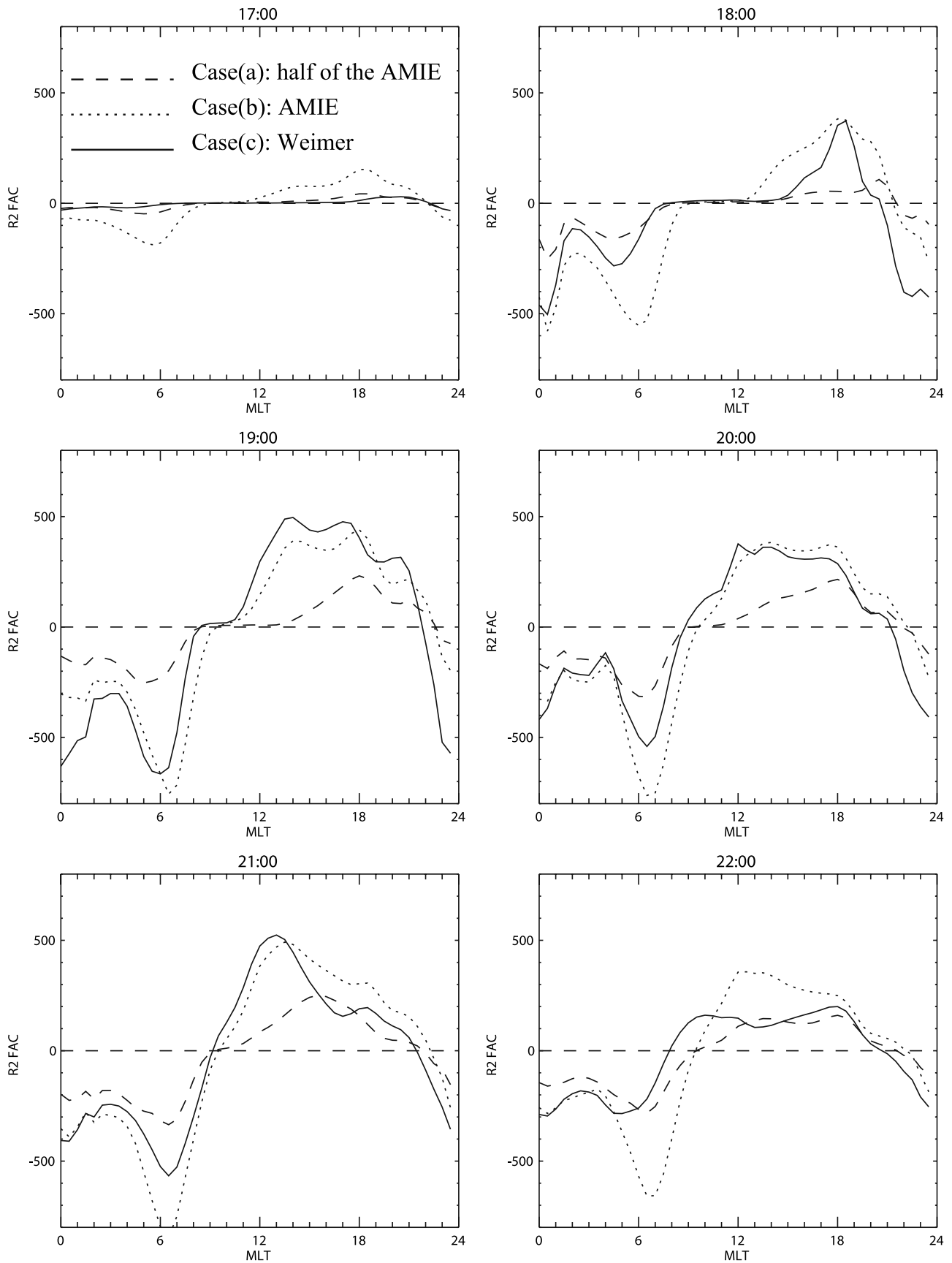


Figure 10. The magnetic local time distribution of the total Region 2 FACs in the ionosphere integrated between the magnetic latitude 40° – 60° (in Ampere) at six different universal times (1700 UT, 1800 UT, 1900 UT, 2000 UT, 2100 UT, and 2200 UT).

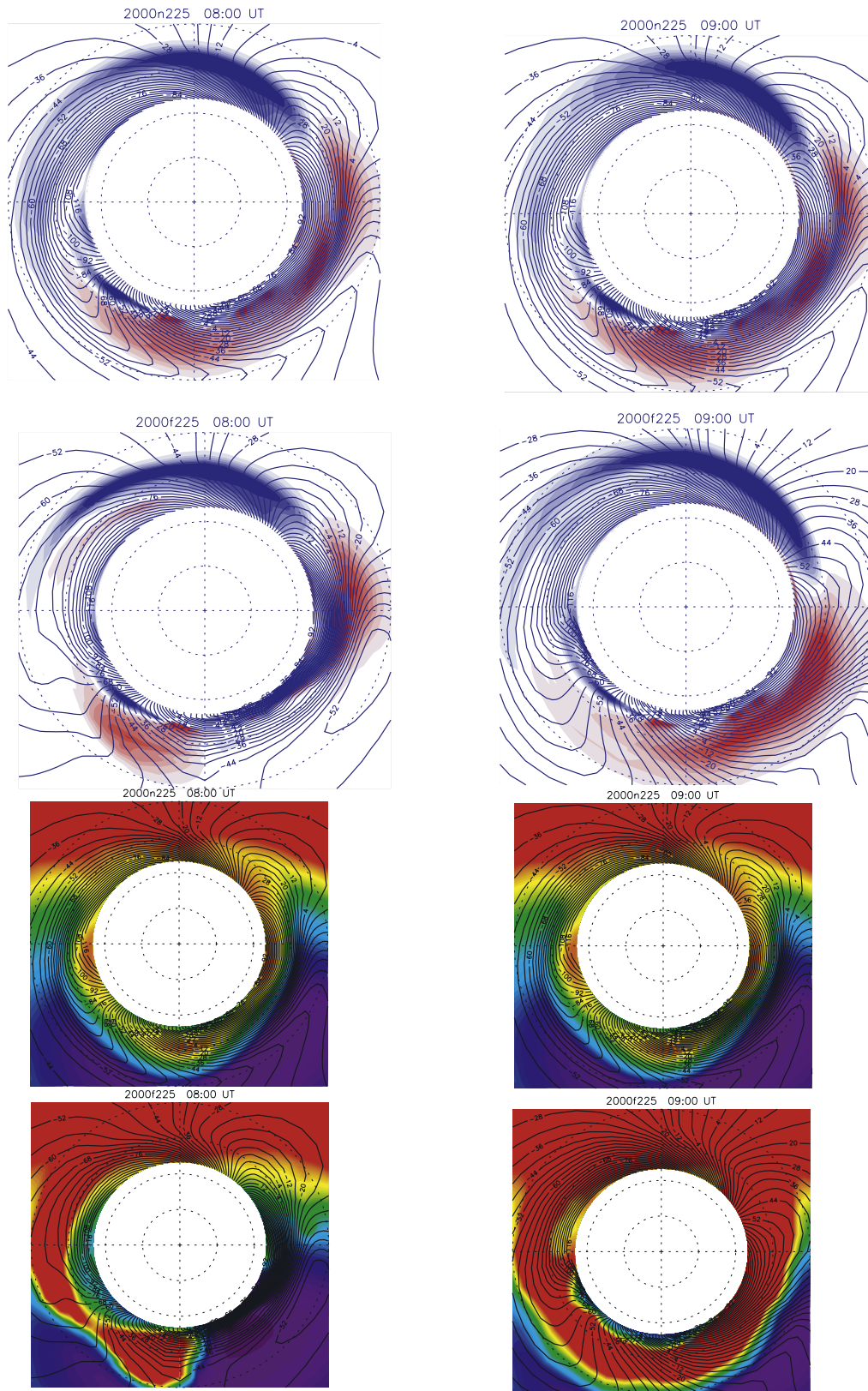


Figure 11. The model comparison of the two runs without or with realistic auroral conductance at two selected times (0800 UT and 0900 UT) near the Dst minimum (0900 UT). The first row shows the FAC map of the reference run (with Hardy model), the second row shows the FAC map of the run using IMAGE/FUV data. The third row shows the auroral Pedersen conductance from both hemispheres used for the reference run, and the fourth row is the auroral Pedersen conductance obtained from the IMAGE/FUV data.

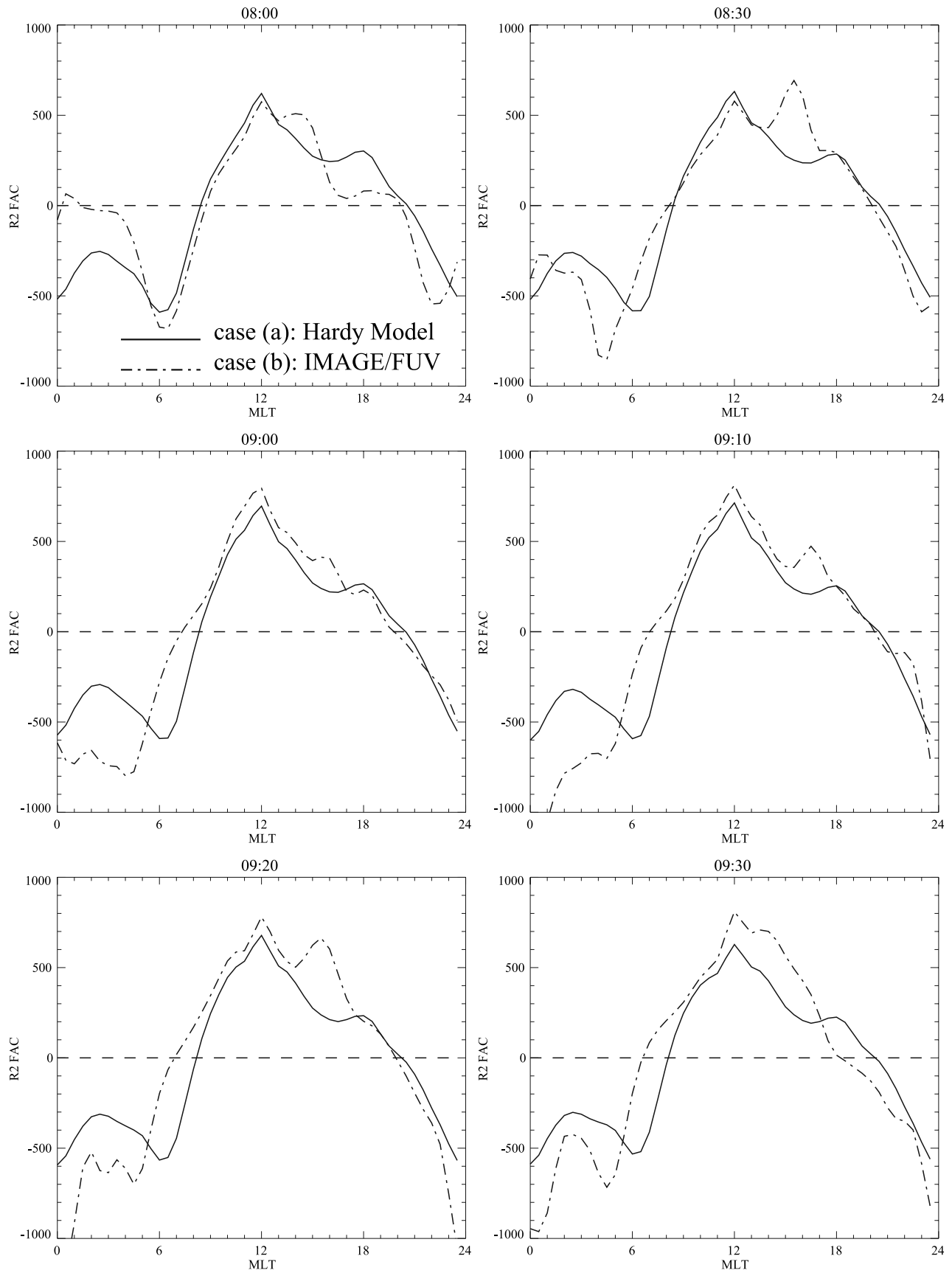


Figure 12. The comparison in the format of Figure 10, magnetic local time distribution of Region 2 FACs at different times, with the solid line representing the reference run and the dashed-dotted line representing the run with FUV data.

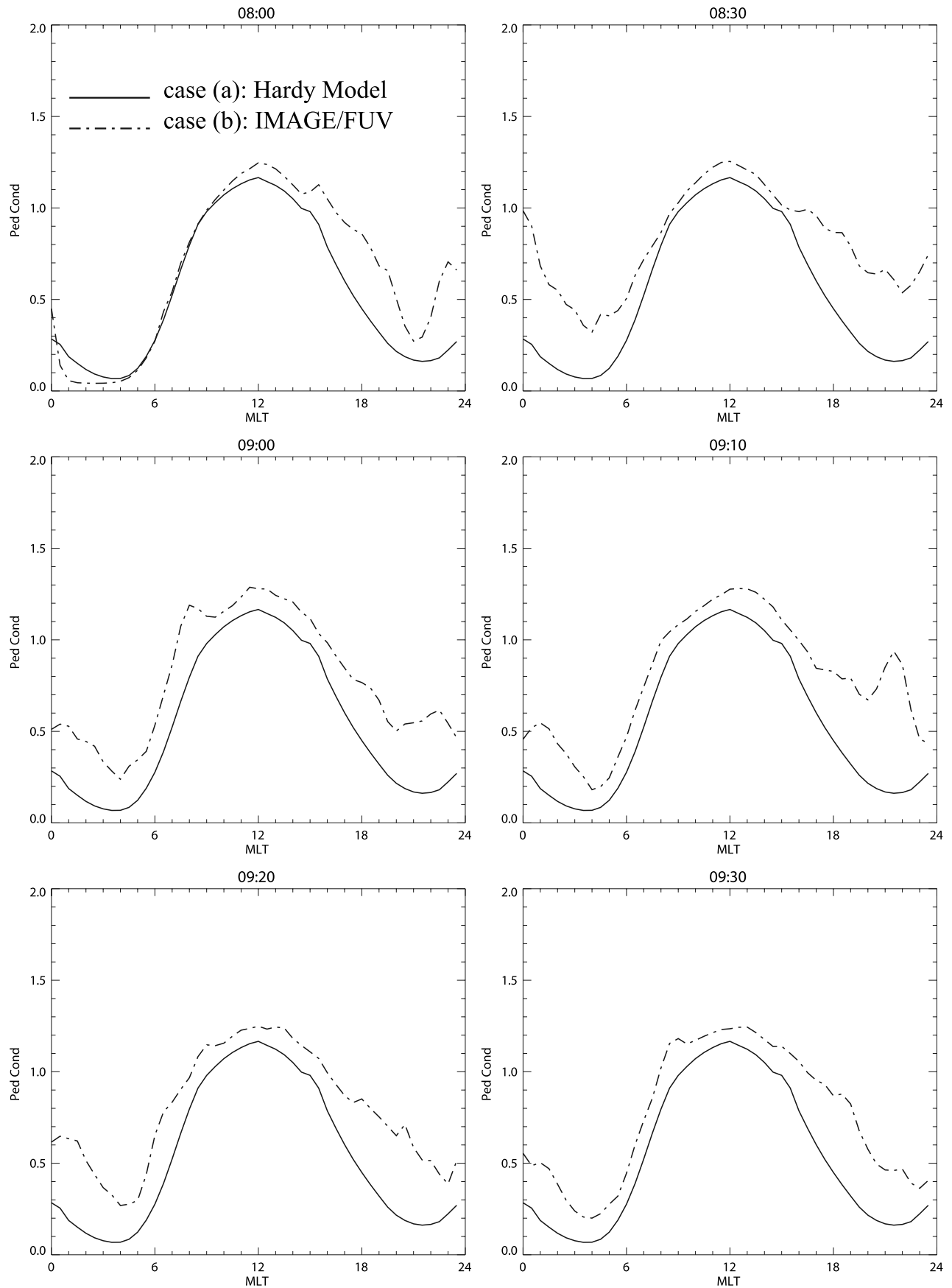


Figure 13. The local time distribution of the “equivalent” auroral Pedersen conductance (Σ_{p_equiv}) defined in equation (12).

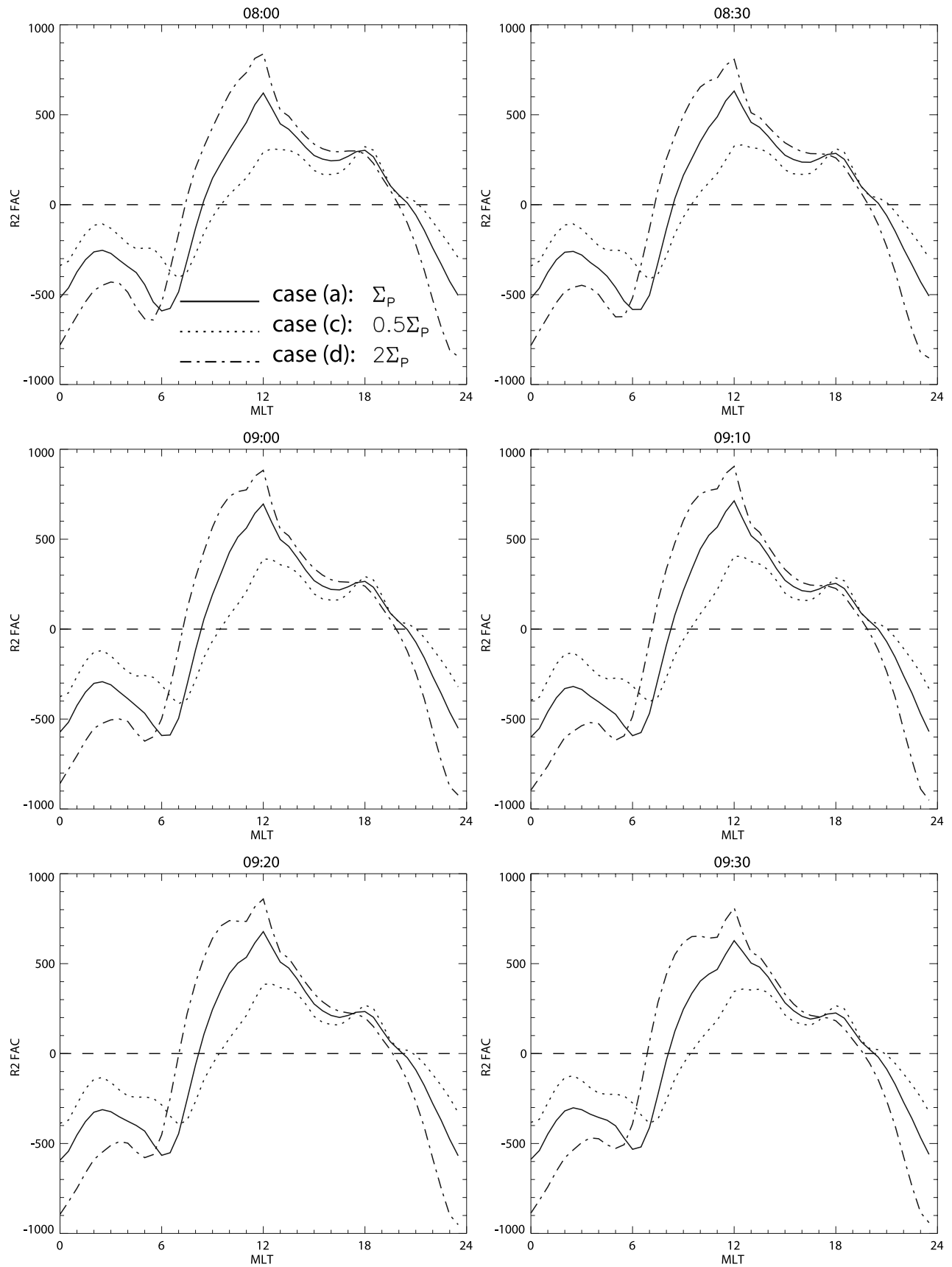


Figure 14. The local time distribution of Region 2 FACs. The reference run is the solid line. The dotted line represents the run whose Pedersen conductance is half of the reference run and the dotted-dashed line represents the run whose Pedersen conductance is twice the reference run.

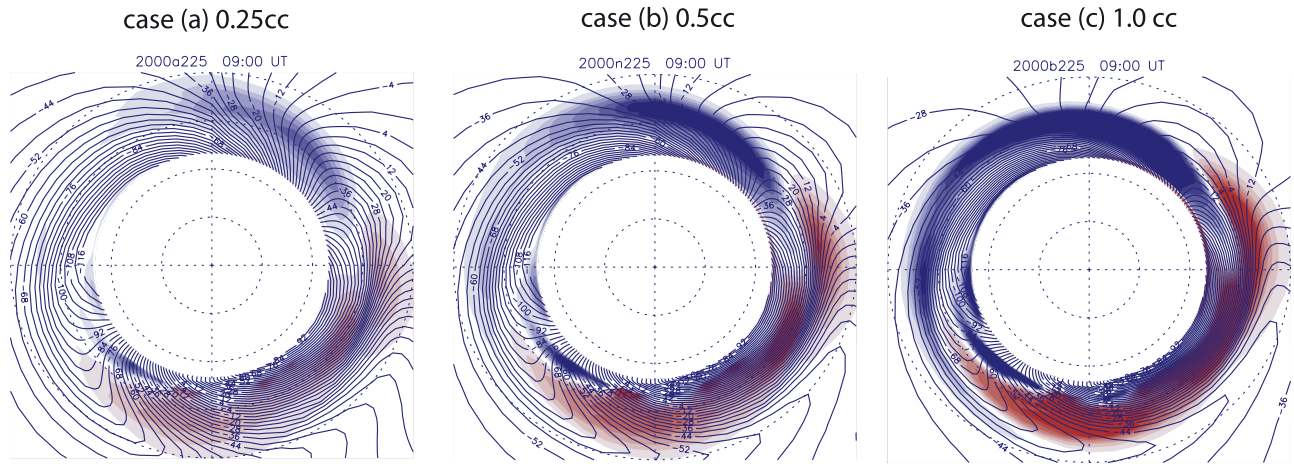


Figure 15. The FAC map is plotted for three different densities in the order of 0.25 cm^{-3} , 0.5 cm^{-3} , and 1.0 cm^{-3} from left to right. The time is at 0900 UT.

two other runs by changing the plasma sheet density only ($N_{PS} = 0.25 \text{ cm}^{-3}$: case (a) and $N_{PS} = 1.0 \text{ cm}^{-3}$: case (c) respectively).

[49] Figure 15 shows the FACs map for three different densities in the order of 0.25 cm^{-3} , 0.5 cm^{-3} , and 1.0 cm^{-3} from left to right. The time is at 0900 UT. The peak of the pressure moves from being closer to Earth to further away from the Earth and shifts more toward 1800 MLT with increasing density (not shown). Region 2 FACs intensify and spread across all local times as the density increases. Figure 15 also indicates an increased shielding in the electric field with increased densities. As the plasma sheet density increases, the strong shielding impedes the inward motion of additional ring current particles, resulting in more outward peaked ring current pressure. As a result, Region 2 FACs have a lesser spread towards lower latitudes, with increasing density. Our analysis also shows that a large plasma sheet density tends to result in stronger electric fields at high latitudes.

[50] The local time distribution of Region 2 FACs at several different times is shown in Figure 16 for the runs with three different densities (0.25 cm^{-3} in the dotted-dash line, 0.5 cm^{-3} in solid and 1.0 cm^{-3} in the dotted line). A large plasma sheet density results in stronger Region 2 FACs at almost all local times. The negative peak in Region 2 FACs (outflowing current) moves more towards dayside with increasing density as stronger shielding electric fields create a more eastward twist of the global potential pattern.

4.4. Effects of Magnetic Field Configuration on Region 2 FACs

[51] In order to highlight the effects of different magnetic field configurations on the development of Region 2 FACs, we performed two runs of the 22 April 2001 storm, one using the T96 model (case a) and the other using the latest Tsyganenko 2004 model for storm times (T04S) (case b) [Tsyganenko and Sitnov, 2005]. All the other parameters stay the same for both runs. The plasma sheet density is taken as a constant (0.5 cm^{-3}) and the plasma sheet temperature is assumed to be 5 keV. The polar cap potential drop is taken from the Weimer 2000 model. For both runs, the magnetic field configuration is updated every 10 minutes according to the ACE measurements. As mentioned above,

the T96 model takes the solar wind dynamic pressure, the Dst index, IMF B_y , and IMF B_z as its input parameters. The T04S model not only takes these parameters as input, but also considers the history of solar wind and IMF conditions, as well as the different response time of magnetospheric current systems (with six other parameters called W_i , $i = 1, 2, 3, 4, 5, 6$).

[52] The equatorial distribution of the ring current perpendicular pressure and the ionospheric distribution of FACs are shown in Figure 17 for two different runs at 1500 UT, which is near the Dst minimum. The top one is for the T96 model and the bottom one is for the T04S model. The perpendicular pressure using the T04S model is much larger than that of the T96 model (notice the difference in color bars) and its peaks are located farther away from the Earth. The Region 2 FACs are more intense with the T04S model than with the T96 model. The intense part of Region 2 FACs has a relatively narrow latitudinal extent with the T04S model, which may be explained by the relatively narrow distribution of the pressure peaks on the left. The Region 2 FACs also display a dawn-dusk asymmetry similar to what is reported by Anderson *et al.* [2005]: the dusk currents shift a few degrees further equatorward than those at dawn. The dawn-dusk asymmetry in the Region 2 FAC intensity can be best viewed in Figure 18, which shows the local time distribution of Region 2 FACs for two runs with the solid line representing the T96 model and the dotted-dashed line representing the T04S model, at 1400 UT, 1500 UT, 1540 UT, 1600 UT, 1700 UT, and 1800 UT respectively.

[53] The equatorial map of db along with the potential contour ($db = |B_{\text{model}}| - |B_{\text{dipole}}|$) at 1500 UT for the two runs are shown in Figure 19 with the top one from the T96 model and the bottom from the T04S model. We can see that the T96 model produces a rather inflated inner magnetosphere with db being mostly negative inside $7 R_E$, reaching -150 nT inside $4 R_E$ on the dayside and $5 R_E$ on the nightside. However, the db is symmetric at dawn and at dusk. In contrast to the db map of the T96 model, the T04S model results in a less inflated magnetosphere (negative db) with the db minimum mostly in the dusk sector (between 1800 and 2400 MLT). This asymmetry in magnetic field configuration may be connected to the asymmetric distri-

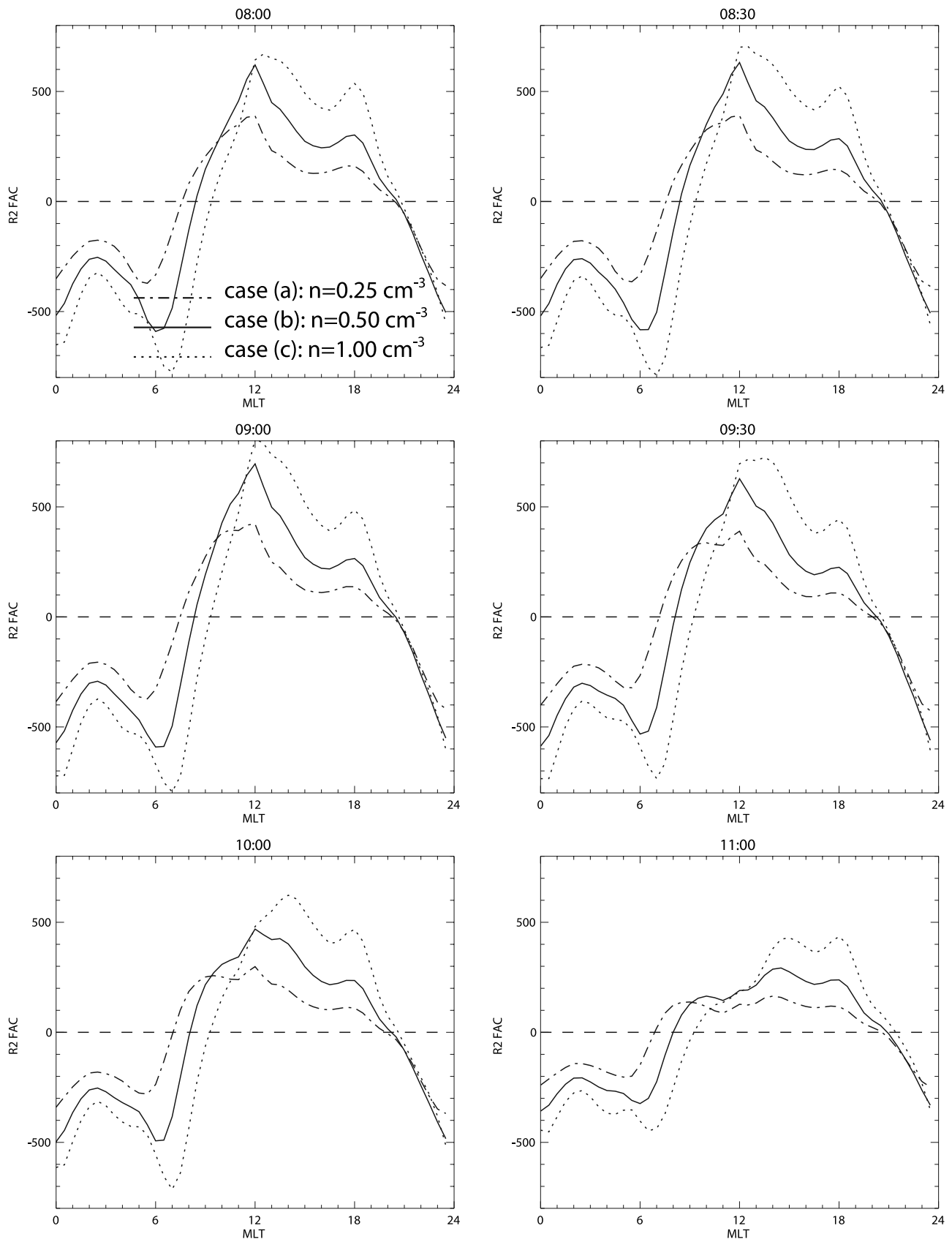


Figure 16. The local time distribution of Region 2 FACs at several different times is shown for the runs with three different densities (0.25 cm^{-3} in dotted-dash line, 0.5 cm^{-3} in solid, and 1.0 cm^{-3} in dotted line).

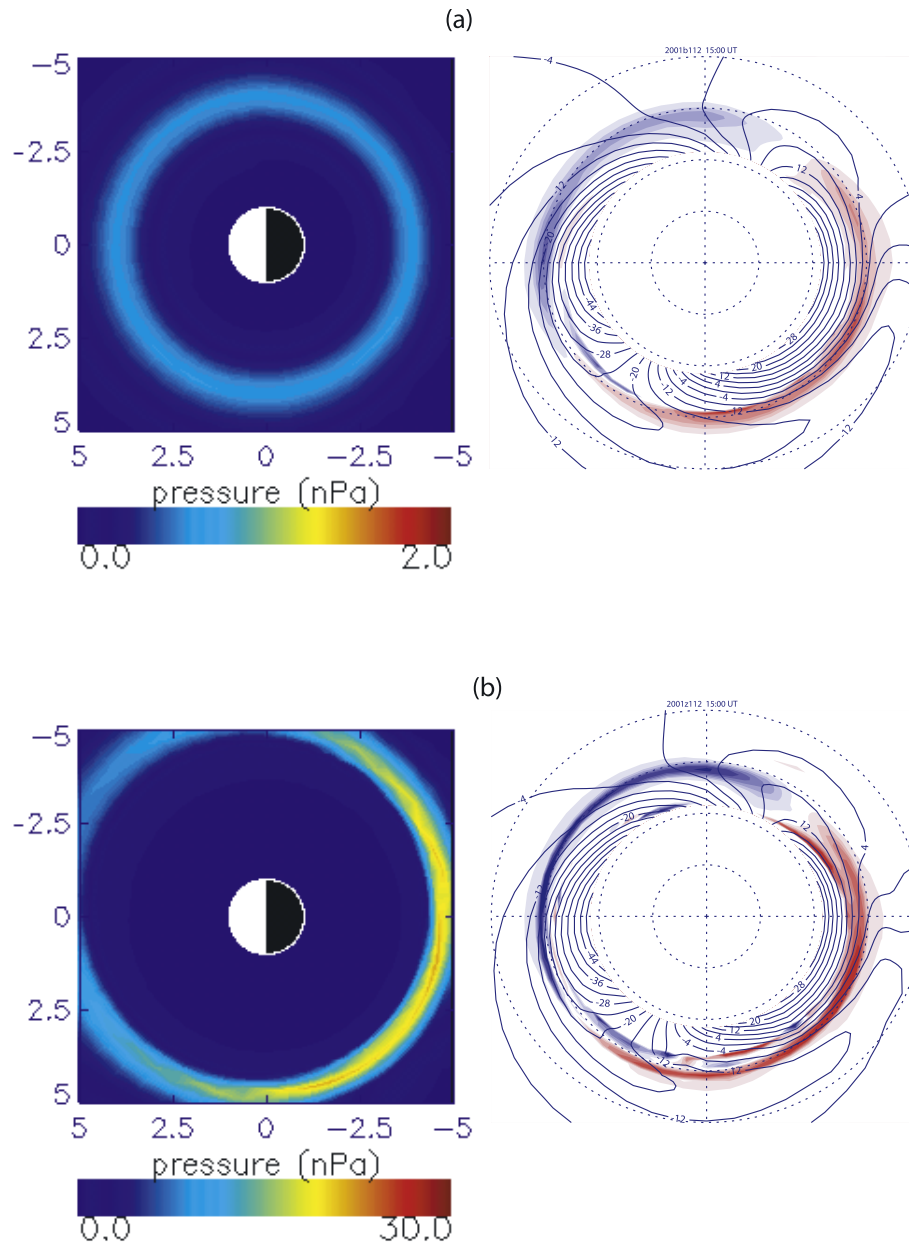


Figure 17. The equatorial distribution of the ring current perpendicular pressure and the ionospheric distribution of FACs are shown here for two different runs at 1500 UT, which is near the Dst minimum. The top one is for the T96 model and the bottom one is for the T04S model.

bution of the ring current pressure (see Figure 17), and ultimately may result in the dawn-dusk asymmetry seen in the large scale Region 2 FACs during storm times.

5. Discussion and Summary

[54] Using the CRCM, we first simulated the two GEM events with different storm intensities and characteristics. We then performed several numerical experiments to investigate the evolution and morphology of Region 2 FACs under the individual influence of several important parameters, such as polar cap potential drop, ionospheric conductivity, plasma sheet density, and different magnetic field models. The simulation results of two GEM events under

the default setting serve as further validation of the CRCM, as they capture major characteristics of Region 2 FACs compared with the Iridium data. The simulated ENA fluxes are also in good agreement with the IMAGE/HENA data. The parametric study shows that an increase in polar cap potential, ionospheric conductivity, or plasma sheet density generally results in an increase in the intensity of Region 2 FACs, but Region 2 FACs have different local time and latitudinal distributions for changes in different parameters due to different mechanisms. A large polar cap potential tends to result in strong and equatorward expanded Region 2 FACs, along with a strong ring current. An increase in ionospheric conductivity reduces the shielding effects and

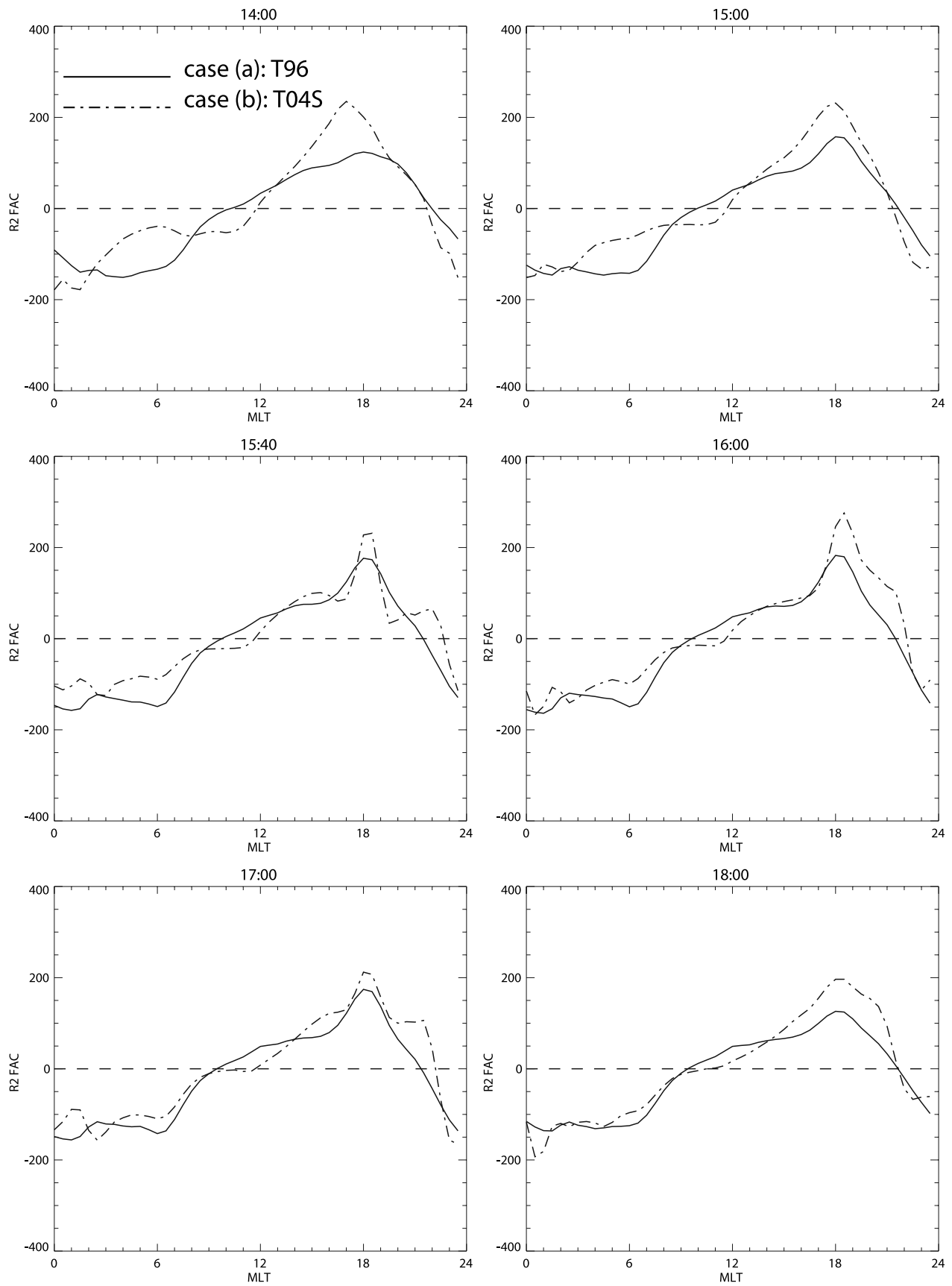


Figure 18. The local time distribution of Region 2 FACs for two runs with the solid line representing the T96 model and the dotted-dashed line representing the T04S model, at 1400 UT, 1500 UT, 1540 UT, 16:00 UT, 1700 UT, and 1800 UT respectively.

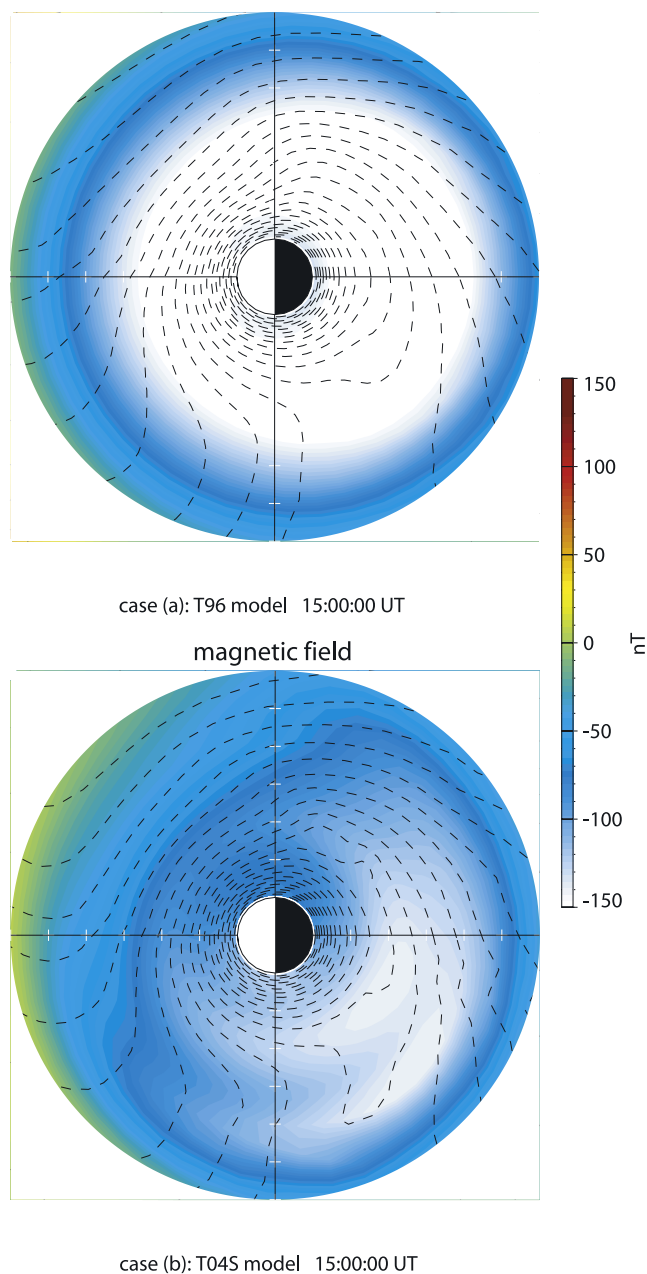


Figure 19. The equatorial map of db along with the potential contour ($db = |B_{\text{model}}| - |B_{\text{dipole}}|$) at 1500 UT for two runs are shown here, with the top one from the T96 model and the bottom from the T04S model.

therefore results in further inward transport of the ring current particles and a stronger ring current. The increased plasma sheet density also results in increased intensity in Region 2 FACs, but with a less equatorward expansion. A large plasma sheet density results in strong shielding electric fields which impede the inward motion of additional ring current particles and therefore result in a more outward peaked ring current pressure. The more outward peaked ring current pressure then leads to a more poleward Region 2 FAC. Please see Figures 10, 14, and 16 for a comparison of the local time distribution of Region 2 FACs under different parameters. Using the CRCM, we have reproduced the

dawn-dusk asymmetry in Region 2 FACs during geomagnetically active times by using the T04S model, which includes a partial ring current. It is found that more intense currents flow into the ionosphere around dusk, compared to those that flow out of the ionosphere around dawn, and the dusk currents shift further equatorward. Our simulation indicates that the dawn-dusk asymmetry in Region 2 FACs can be explained by the interactions of the asymmetric inflation of the magnetic field on the dusk and the asymmetric distribution in ring current population.

[55] It is known that the magnetosphere and ionosphere are a highly coupled and complex system. The morphology and intensity of Region 2 FACs are regulated by multiple factors, such as external factors representing the strength of solar wind and magnetosphere coupling, ionospheric conductivity (a partially internal factor), ring current particle source strength, magnetic field and electric field configurations, etc. Any change that affects the electrodynamic coupling of the magnetosphere-ionosphere can result in changes in Region 2 FACs, especially those that affect the development of ring current. The location of Region 2 FACs is closely related to the location of the ring current pressure.

[56] Currently, it remains difficult to study the relationship between the Region 2 FACs and the ring current from a global perspective due to lack of measurements. Model results from the CRCM, which includes the M-I coupling, complement our capability in understanding the complexity of the system, despite the limitations of the model. The numerical experiments of the parametric study allow us to gain insights into the physical mechanisms involved in the relationship of the Region 2 FACs and the ring current by varying one major parameter and keeping the others constant. The two GEM events show that the evolution of Region 2 FACs depends both on the intensity and the specific phase of a storm: a large negative Dst tends to connect with more equatorward expanded and more intense Region 2 FACs, and correspondingly the ring current particles usually penetrate deeper into the inner magnetosphere. The complicated nature of the relationship between two current systems is also manifested in the nonlinearity of various controlling factors on the development of Region 2 FACs through the simulation results, with each parameter having different effects on its morphology and intensity. This study serves as a baseline assessment of the complex relationship between Region 2 FACs and the ring current. Similar modeling efforts with more realistic boundary conditions based on observations (both for the cross-polar cap potential representation at the high latitude boundary and for the source population of the ring current) and more numerical experiments by varying parameters in a more complicated fashion (such as considering local time distribution of the aforementioned parameters) are needed to further our understanding of the electrodynamic coupling of the inner magnetosphere and ionosphere and our understanding of the two major current systems.

[57] **Acknowledgments.** We thank two reviewers for their constructive and substantive comments. ACE data were obtained from CDAWEB and Dst index was provided from the World Data Center for Geomagnetism in Kyoto, Japan. We thank the whole IMAGE team for making it a success and for the data. We thank R. A. Wolf and his coworkers for the development of RCM. Y. Z. wants to thank Yusuke Ebihara for his help

with some of the plotting software. This work was supported by a NASA grant to JHU/APL.

References

- Anderson, B. J., K. Takahashi, and B. A. Toth (2000), Sensing global Birkeland currents with Iridium engineering magnetometer data, *Geophys. Res. Lett.*, **27**, 4045.
- Anderson, B. J., K. Takahashi, T. Kamei, C. L. Walters, and B. A. Toth (2002), Birkeland current system key parameters derived from Iridium observations: Method and initial validation results, *J. Geophys. Res.*, **107**(A6), 1079, doi:10.1029/2001JA000080.
- Anderson, B. J., S.-I. Ohtani, H. Korth, and A. Ukhorskiy (2005), Storm time dawn-dusk asymmetry of the large-scale Birkeland currents, *J. Geophys. Res.*, **110**, A12220, doi:10.1029/2005JA011246.
- Atkinson, G., and D. Hutchison (1978), Effect of the day night ionospheric conductivity gradient on polar cap convective flow, *J. Geophys. Res.*, **83**, 725.
- Bilitza, D. (1997), International reference ionosphere-Status, 1995/96, *Adv. Space Res.*, **20**, 1751.
- Borovsky, J. E., M. F. Thomsen, and R. C. Elphic (1998), The driving of the plasma sheet by the solar wind, *J. Geophys. Res.*, **103**, 17,617.
- Brandt, P. C., S. Ohtani, D. G. Mitchell, M.-C. Fok, E. C. Roelof, and R. Demajistre (2002), Global ENA observations of the storm main-phase ring current: Implications for skewed electric fields in the inner magnetosphere, *Geophys. Res. Lett.*, **29**(20), 1954, doi:10.1029/2002GL015160.
- Chen, M. W., M. Schulz, L. R. Lyons, and D. J. Gorney (1993), Stormtime transport of ring current and radiation belt ions, *J. Geophys. Res.*, **98**, 3835.
- Chen, M. W., L. R. Lyons, and M. Schulz (1994), Simulations of phase space distributions of storm time proton ring current, *J. Geophys. Res.*, **99**, 5745.
- Daglis, I. A., R. M. Thorne, W. Baumjohann, and S. Orsini (1999), The terrestrial ring current: Origin, formation, and decay, *Rev. Geophys.*, **37**, 407.
- Ebihara, Y., and M. Ejiri (2002), Numerical simulation of the ring current: Review, *Space Sci. Rev.*, **105**, 377.
- Ebihara, Y., and M. C. Fok (2004), Postmidnight storm-time enhancement of tens-of-keV proton flux, *J. Geophys. Res.*, **109**, A12209, doi:10.1029/2004JA010523.
- Ebihara, Y., M. C. Fok, R. A. Wolf, T. J. Immel, and T. E. Moore (2004), Influence of ionosphere conductivity on the ring current, *J. Geophys. Res.*, **109**, A08205, doi:10.1029/2003JA010351.
- Ebihara, Y., M. C. Fok, R. A. Wolf, M. F. Thomsen, and T. E. Moore (2005), Nonlinear impact of plasma sheet density on the storm-time ring current, *J. Geophys. Res.*, **110**, A02208, doi:10.1029/2004JA010435.
- Ejiri, M., R. A. Hoffmann, and P. H. Smith (1978), The convection electric field model for the magnetosphere based on Explorer 45 observations, *J. Geophys. Res.*, **83**, 4911.
- Erlanson, R. E., L. J. Zanetti, T. A. Potemra, P. F. Bythrow, and R. Lundin (1988), IMF By dependence of region 1 Birkeland currents near noon, *J. Geophys. Res.*, **93**, 9804.
- Fejer, B. G., R. W. Spiro, R. A. Wolf, and J. C. Foster (1990), Latitudinal variation of perturbation electric fields during magnetically disturbed periods: 1986 SUNDIAL observations and model results, *Ann. Geophys.*, **8**, 441.
- Fok, M. C., and T. E. Moore (1997), Ring current modeling in a realistic magnetic field configuration, *Geophys. Res. Lett.*, **24**, 1775.
- Fok, M.-C., J. U. Kozyra, A. F. Nagy, C. E. Rasmussen, and G. V. Khazanov (1993), Decay of equatorial ring current ions and associated aeronomical consequences, *J. Geophys. Res.*, **98**, 19,381.
- Fok, M.-C., T. E. Moore, and M. E. Greenspan (1996), Ring current development during storm main phase, *J. Geophys. Res.*, **101**, 15,311.
- Fok, M.-C., T. E. Moore, and D. C. Delcourt (1999), Modeling of inner plasma sheet and ring current during substorms, *J. Geophys. Res.*, **104**, 14,557.
- Fok, M.-C., R. A. Wolf, R. W. Spiro, and T. E. Moore (2001a), Comprehensive computational model of the Earth's ring current, *J. Geophys. Res.*, **106**, 8417.
- Fok, M.-C., T. E. Moore, and W. N. Spiedvik (2001b), Rapid enhancement of radiation belt electron fluxes due to substorm dipolarization of the geomagnetic field, *J. Geophys. Res.*, **106**, 3873.
- Fok, M.-C., et al. (2003), Global ENA IMAGE simulations, *Space Sci. Rev.*, **109**, 77.
- Fujii, R., and T. Iijima (1987), Control of ionospheric conductivities on large-scale Birkeland current intensities under geomagnetic quiet conditions, *J. Geophys. Res.*, **92**, 4505.
- Hardy, D. A., M. S. Gussenhoven, R. Raistrick, and W. J. McNeil (1987), Statistical and functional representations of the pattern of auroral energy flux, number flux and conductivity, *J. Geophys. Res.*, **92**, 12,275.
- Harel, M., R. A. Wolf, P. H. Reiff, R. W. Spiro, W. J. Burke, F. J. Rich, and M. Smiddy (1981), Quantitative simulation of a magnetospheric substorm: 1. Model logic and overview, *J. Geophys. Res.*, **86**, 2217.
- Iijima, T. (1984), Field-aligned currents during northward IMF, in *Magnetospheric Currents*, *Geophys. Monogr. Ser.*, vol. 28, edited by T. A. Potemra, pp. 115–122, AGU, Washington, D. C.
- Iijima, T., and T. A. Potemra (1978), Large-scale characteristic of field-aligned currents at northern high latitudes observed by Triad, *J. Geophys. Res.*, **83**, 599.
- Jaggi, R. K., and R. A. Wolf (1973), Self-consistent calculation of the motion of a sheet of ions in the magnetosphere, *J. Geophys. Res.*, **78**, 2852–2866.
- Jordanova, V. K. (2003), New insights on geomagnetic storms from model simulations using multi-spacecraft data, *Space Sci. Rev.*, **107**, 157.
- Jordanova, V. K., J. U. Kozyra, A. F. Nagy, and G. V. Khazanov (1997), Kinetic model of ring current–atmosphere interactions, *J. Geophys. Res.*, **102**, 14,279.
- Korth, H., B. J. Anderson, M. J. Wiltberger, J. G. Lyon, and P. C. Anderson (2004), Intercomparison of ionospheric electrodynamics from the Iridium constellation with global MHD simulations, *J. Geophys. Res.*, **109**, A07307, doi:10.1029/2004JA010428.
- Kozyra, J. U., and M. W. Liemohn (2003), Ring current energy input and decay, *Space Sci. Rev.*, **109**, 105–131.
- Liemohn, M. W., J. U. Kozyra, V. K. Jordanova, G. V. Khazanov, M. F. Thomsen, and T. E. Cayton (1999), Analysis of early phase ring current recovery mechanisms during geomagnetic storms, *Geophys. Res. Lett.*, **25**, 2845.
- Liemohn, M. W., A. J. Ridley, P. C. Brandt, D. L. Gallagher, J. U. Kozyra, D. M. Ober, D. G. Mitchell, E. C. Roelof, and R. Demajistre (2005), Parametric analysis of nightside conduction effects on inner magnetospheric dynamics for the 17 April 2002 storm, *J. Geophys. Res.*, **110**, A12S22, doi:10.1029/2005JA011109.
- Mende, S. B., et al. (2000a), Far ultraviolet imaging from the IMAGE spacecraft, 2. Wideband FUV imaging, *Space Sci. Rev.*, **91**, 271.
- Mende, S. B., et al. (2000b), Far ultraviolet imaging from the IMAGE spacecraft, 3. Spectral imaging of Lyman- α and OI 135.6 nm, *Space Sci. Rev.*, **91**, 287.
- Mitchell, D. G., et al. (2000), High energy neutral atom (HENA) imager for the IMAGE mission, *Space Sci. Rev.*, **91**, 67.
- Ohtani, S., G. Ueno, T. Higuchi, and H. Kawano (2005), Annual and semiannual variations of the location and intensity of large-scale field-aligned currents, *J. Geophys. Res.*, **110**, A01216, doi:10.1029/2004JA010634.
- Peymirat, C., A. D. Richmond, B. A. Emery, and R. G. Roble (1998), A magnetosphere-ionosphere-thermosphere electrodynamic general circulation model, *J. Geophys. Res.*, **103**, 17,467.
- Peymirat, C., A. D. Richmond, and A. T. Koba (2000), Electrodynamic coupling of high and low latitudes: Simulations of shielding and over-shielding effects, *J. Geophys. Res.*, **105**, 22,991.
- Richmond, A. D. (1992), Assimilative mapping of ionospheric electrodynamic, *Adv. Space Sci.*, **12**, 669.
- Ridley, A. J., T. I. Gombosi, and D. L. DeZeeuw (2004), Ionospheric control of the magnetosphere: Conductance, *Ann. Geophys.*, **22**, 567.
- Russell, C. T., and M. Fleishman (2002), Joint control of region-2 field-aligned currents by the east-west component of the interplanetary electric field and polar cap illumination, *J. Atmos. Sol. Terr. Phys.*, **64**, 1803.
- Senior, C., and M. Blanc (1984), On the control of magnetospheric convection by the spatial distribution of ionospheric conductivities, *J. Geophys. Res.*, **89**, 261.
- Sheldon, R. B., and D. C. Hamilton (1993), Ion transport and loss in the Earth's quiet ring current, 1, Data and standard model, *J. Geophys. Res.*, **98**, 13,491.
- Siscoe, G. L., G. M. Erickson, B. U. Ö. Sonnerup, N. C. Maynard, J. A. Schoendorf, K. D. Siebert, D. R. Weimer, W. W. White, and G. R. Wilson (2002), Hill model of transpolar potential saturation: Comparisons with MHD simulations, *J. Geophys. Res.*, **107**(A6), 1075, doi:10.1029/2001JA000109.
- Southwood, D. J. (1977), The role of hot plasma in magnetospheric convection, *J. Geophys. Res.*, **82**, 5512.
- Spiro, R. W., and R. A. Wolf (1984), Electrodynamics of convection in the inner magnetosphere, in *Magnetospheric Currents*, *Geophys. Monogr. Ser.*, vol. 28, edited by T. A. Potemra, p. 248, AGU, Washington, D. C.
- Spiro, R. W., M. Harel, R. A. Wolf, and P. H. Reiff (1981), Quantitative simulation of a magnetospheric substorm: 3. Plasmaspheric electric fields and evolution of the plasmopause, *J. Geophys. Res.*, **86**, 2261.
- Spiro, R. W., R. A. Wolf, and B. G. Fejer (1988), Penetration of high-latitude-electric-field effects to low latitudes during SUNDIAL 1984, *Ann. Geophys.*, **6**, 39.
- Tanaka, T. (1995), Generation mechanisms for magnetosphere-ionosphere current system deduced from a three-dimensional MHD simulation of a

- solar wind-magnetosphere-ionosphere coupling processes, *J. Geophys. Res.*, *100*, 12,057.
- Toffoletto, F., S. Sazykin, R. Spiro, and R. Wolf (2003), Inner magnetosphere modeling with the Rice Convection Model, *Space Sci. Rev.*, *107*, 175.
- Tsyganenko, N. A. (1995), Modeling the Earth's magnetospheric magnetic field confined within a realistic magnetopause, *J. Geophys. Res.*, *100*, 5599.
- Tsyganenko, N. A., and I. M. Sitnov (2005), Modeling the dynamics of the inner magnetosphere during strong geomagnetic storms, *J. Geophys. Res.*, *110*, A03208, doi:10.1029/2004JA010798.
- Vasyliunas, V. M. (1970), Mathematical models of magnetospheric convection and its coupling to the ionosphere, in *Particles and Fields in the Magnetosphere*, edited by B. M. McCormac, pp. 60–71, Springer, New York.
- Vasyliunas, V. M. (1972), The interrelationship of magnetospheric processes, in *Earth's Magnetosphere Processes*, edited by B. M. McCormac, pp. 29–38, Springer, New York.
- Wang, H., H. Luhr, and S. Y. Ma (2005), Solar zenith angle and merging electric field control of field-aligned currents: A statistical study of the southern hemisphere, *J. Geophys. Res.*, *110*, A03306, doi:10.1029/2004JA010530.
- Waters, C. L., B. J. Anderson, and K. Liou (2001), Estimation of global field aligned currents using Iridium magnetometer data, *Geophys. Res. Lett.*, *28*, 2165.
- Weimer, D. R. (2001), An improved model of ionospheric electric potentials including substorm perturbations and application to the Geospace Environment Modeling November 24, 1996, event, *J. Geophys. Res.*, *106*, 407.
- Wolf, R. A. (1970), Effects of ionospheric conductivity on convection flow of plasma in the magnetosphere, *J. Geophys. Res.*, *75*, 4677.
- Wolf, R. A., M. Harel, R. W. Spiro, G.-H. Voigt, P. H. Reiff, and C. K. Chen (1982), Computer simulation of inner magnetospheric dynamics for the magnetic storm of July 29, 1977, *J. Geophys. Res.*, *87*, 5949.
- Zanetti, L. J., W. Baumjohann, and T. A. Potemra (1983), Ionospheric and Birkeland current distributions inferred from the MAGSAT magnetometer data, *J. Geophys. Res.*, *88*, 4875.
- Zheng, Y., M.-C. Fok, and G. V. Khazanov (2003), A radiation belt-ring current forecasting model, *Space Weather*, *1*(3), 1013, doi:10.1029/2003SW000007.

B. J. Anderson, P. C. Brandt, A. T. Y. Lui, D. G. Mitchell, and Y. Zheng, Johns Hopkins University Applied Physics Laboratory, Laurel, MD 20723-6099, USA. (brian.anderson@jhuapl.edu; brandpc1@jhuapl.edu; tony.liu@jhuapl.edu; donald.g.mitchell@jhuapl.edu; yihua.zheng@jhuapl.edu)
 M. C. Fok, NASA Goddard Space Flight Center, Code 612.2, Greenbelt, MD 20771, USA. (mei-ching.h.fok@nasa.gov)
 T. J. Immel, Space Science Laboratory, University of California, Berkeley, Centennial Drive at Grizzly Peak Blvd., Berkeley, CA 94720-7450, USA. (immed@ssl.berkeley.edu)